

Contract N00014-87-C-0363

QUANTUM DEVICE DEVELOPMENT

AD-A201 948

Texas Instruments Incorporated
Central Research Laboratories
P.O. Box 655936
Dallas, Texas 75265

DTIC
ELECTE
NOV 30 1988
S D
C&D

12 October 1988

Interim Technical Report for 4 September 1987 - 31 August 1988

~~Restriction limited to U.S. Government Agencies
and qualified U.S. DoD contractors (MIL 6817 7/15/87)~~

Disclaimer

The views and conclusions contained in this document are those of the authors and should not be interpreted as necessarily representing the official policies, either expressed or implied, of the Defense Advanced Research Projects Agency or the United States Government.

Prepared for
Office of Naval Research
800 North Quincy Street
Arlington, Virginia 22217-5000

DISTRIBUTION STATEMENT A
Approved for public release
Distribution Unlimited

REPORT DOCUMENTATION PAGE

1a. REPORT SECURITY CLASSIFICATION Unclassified			1b. RESTRICTIVE MARKINGS			
2a. SECURITY CLASSIFICATION AUTHORITY			3. DISTRIBUTION/AVAILABILITY OF REPORT Distribution limited to U.S. Government Agencies and qualified U.S. MOD contractors (MIL CRI 7/15/87).			
2b. DECLASSIFICATION/DOWNGRADING SCHEDULE						
4. PERFORMING ORGANIZATION REPORT NUMBER(S) 08-88-55			5. MONITORING ORGANIZATION REPORT NUMBER(S) ONR			
6a. NAME OF PERFORMING ORGANIZATION Texas Instruments Incorporated		6b. OFFICE SYMBOL <i>(if applicable)</i>	7a. NAME OF MONITORING ORGANIZATION ONR			
6c. ADDRESS (City, State, and Zip Code) Dallas, Texas 75265			7b. ADDRESS (City, State, and Zip Code) 800 North Quincy St; Arlington, VA 22217			
8a. NAME OF FUNDING/SPONSORING ORG. ONR		8b. OFFICE SYMBOL <i>(if applicable)</i>	9. PROCUREMENT INSTRUMENT IDENTIFICATION NUMBER N00014-87-C-0363			
8c. ADDRESS (City, State, and Zip Code) Attn: LRC, Code; 1114SS Arlington, VA 22217-5000			10. SOURCE OF FUNDING NUMBERS			
			PROGRAM ELEMENT NO.	PROJECT NO.	TASK NO.	WORK UNIT ACCESSION NO.
11. TITLE (Include Security Classification) Quantum Device Development						
12. PERSONAL AUTHOR(S) R.T. Bate, W.R. Frensley, J.H. Luscombe, J.N. Randall, M.A. Reed, A. Seabaugh, C.H. Yang						
13a. TYPE OF REPORT Interim		13b. TIME COVERED 9-4-87/8-31-88		14. DATE OF REPORT (Year, Month, Day) 88-1C-25		
15. PAGE COUNT 93						
16. SUPPLEMENTARY NOTATION						
17. COSATI CODES			18. SUBJECT TERMS (Continue on reverse if necessary and identify by block number)			
FIELD	GROUP	SUB-GROUP	Semiconductor Devices; Gallium Arsenide Devices; Heterojunction Transistors; Resonant Tunneling Transistors; Quantum Semiconductor Devices; Resonant			
19. ABSTRACT (Continue on reverse side if necessary and identify by block number) The results of the first year of research on and development of resonant tunneling transistors are described. Unlike some devices that have been called "resonant tunneling transistors," which are really conventional devices incorporating resonant tunneling diode structures, these are "true" resonant tunneling transistors. A true resonant tunneling transistor consists of a single-well, double-barrier resonant tunneling diode structure to which a third terminal, directly contacting the quantum well, has been added. Two types						
20. DISTRIBUTION/AVAILABILITY OF ABSTRACT <input type="checkbox"/> UNCLASSIFIED/UNLIMITED <input type="checkbox"/> SAME AS RPT. <input type="checkbox"/> DTIC USERS			21. ABSTRACT SECURITY CLASSIFICATION UNCLASSIFIED			
22a. NAME OF RESPONSIBLE INDIVIDUAL Larry R. Cooper			22b. TELEPHONE (Include Area Code) (202) 696-4215		22c. OFFICE SYMBOL	

18. Subject Terms

Tunneling, Molecular Beam Epitaxy, Quantum Transport Theory

19. Abstract (Continued)

of resonant tunneling transistors (RTT) are included within the scope of the contract: a unipolar version called the Quantum Excited-State Tunneling Transistor (QuESTT), and a pseudomorphic bipolar version called the Bipolar Quantum Resonant Tunneling Transistor (BiQuaRTT). A lattice-matched version of the BiQuaRTT has been developed at TI under an earlier Air Force contract. Although the bipolar devices do not meet the downscaling requirements, they require less difficult processing and can serve as a valuable proof of principle and guide to the design of unipolar devices.

The report describes the development of a theory of resonant tunneling structures and its use to derive device models that have been used in the design of device structures. It also describes the extensive process development required to permit contacting the very thin (50 Å) quantum well base layers, and also to isolate the emitter, base, and collector layers. The processes developed have been used to fabricate transistors, and these devices have been characterized electrically. The characterization reveals that a pseudomorphic BiQuaRTT that shows transistor action with a current gain of 5 has been fabricated. Achievement of a functional QuESTT is thought to be imminent.

The report discusses plans for the immediate future in modeling, process development, and device fabrication/characterization efforts, and concludes with recommendations for the remainder of the contract period.



DTIC	CRAB	<input checked="" type="checkbox"/>
DTIC	TAB	<input type="checkbox"/>
DTIC	...	<input type="checkbox"/>
By <i>per ltr</i>		
A-1		

TABLE OF CONTENTS

<u>SECTION</u>		<u>PAGE</u>
	SUMMARY	1
I.	INTRODUCTION.	3
	A. Need for Quantum Devices/Circuits	3
	B. Resonant Tunneling.	5
	C. Resonant-Tunneling Transistors.	7
	1. Quantum-Classical Hybrid Devices.	7
	2. True RTTs	7
II.	PROGRESS/PLANS.	16
	A. Device Theory	16
	1. Device Models	16
	2. Physics of Tunneling Heterostructures	22
	a. Wavepacket Calculations	22
	b. Quantum Transport Theory.	29
	c. Scattering-State Calculations	33
	B. Device Development.	37
	1. Process Development	37
	a. General Processing And Design Constraints	37
	b. Contact To Well (Base).	38
	c. Emitter Contact	39
	d. Collector Contact	39
	e. Base-Emitter Isolation.	39
	f. Isolation, Passivation, And Final Metal	42
	g. Two Base Contact Device	42
	h. Test Structures	42
	2. Pseudomorphic BiQuaRTT.	42
	a. Contact To Well	42
	b. The Epitaxial Structure Of The BiQuaRTT	43
	c. Redesigned Epitaxial Structure.	49
	(1) Structure A--Deep Well BiQuaRTT. Lightly Doped Collector	49

TABLE OF CONTENTS

(Continued)

<u>SECTION</u>	<u>PAGE</u>
(2) Structure B--Wide Well BiQuaRTT, Lightly Doped Collector	49
(3) Structure C--Wide Well BiQuaRTT, Raised & Lightly Doped Collector	50
(4) Variation of Structure B.	50
d. BiQuaRTT Device Results	53
3. QuESTT.	53
a. Baseline Structure.	53
(1) Progress.	53
b. Variations.	58
(1) MBE Thermal Etch And Regrowth	58
(2) Isolation Etch Stop	60
(3) Plans	63
III. CONCLUSIONS/RECOMMENDATIONS	64
REFERENCES.	65

APPENDIXES

- A REALIZATION OF A THREE-TERMINAL RESONANT TUNNELING DEVICE: THE BIPOLAR QUANTUM RESONANT TUNNELING TRANSISTOR (BiQuaRTT)
- B SELECTIVE REACTIVE ION ETCHING OF GaAs ON AlGaAs USING CCl_2F_2 AND HE
- C DEFINITIONS/ACRONYMS

LIST OF ILLUSTRATIONS

<u>FIGURE</u>		<u>PAGE</u>
1.	Characteristics and conduction-band profile of a resonant-tunneling diode.	6
2.	I(V) characteristic of a series combination of a RTD and MOSFET	8
3.	Hot-Electron Tunneling Transistor	10
4.	Quantum Excited-State Tunneling Transistor.	12
5.	Bipolar Tunneling Transistor.	13
6.	Bipolar Quantum Resonant Tunneling Transistor	14
7.	Results of a typical run of the BiQuaRTT modeling program BIQMODEL.	18
8.	Output of QUESTTMOD	19
9.	Scattering-theory I(V) curves for laterally-confined structures.	21
10.	Time evolution of an electron wavepacket escaping from a quantum well by tunneling	23
11.	Results of a simulation of the escape of a wavepacket from a quantum well	25
12.	Results of a simulation of the transmission of a wavepacket through a quantum well.	28
13.	Self-consistent simulations of a resonant-tunneling diode using the Wigner distribution	31
14.	Comparison of the I(V) curves obtained from the Wigner-function and scattering theory calculations.	35
15.	SEM of BiQuaRTT device showing emitter, base, and collector contacts.	40
16.	Multiple trace I-V curves of conduction through p-well with implanted contacts at various spacing	44
17.	Current-voltage characteristics at 77 K of 50 Å In _y Ga _{1-y} As quantum well/40 Å Al _{0.25} G _{0.75} As barrier structures, with y = 0, y ~ 0.03, and y ~ 0.08	45

LIST OF ILLUSTRATIONS
(continued)

<u>FIGURE</u>		<u>PAGE</u>
18.	Current-voltage characteristics at 77 K of (a) an 85 Å GaAs quantum well/35 Å AlAs barrier structure (the ground and first excited state resonances are visible), and (b) an identical structure as in (a), with the replacement of the GaAs quantum well with an 85 Å In _{0.1} Ga _{0.9} As quantum well . . .	46
19.	Equilibrium potential and charge density profiles for the pseudomorphic BiQuaRTT.	51
20.	Room-temperature common-emitter transistor characteristics for the pseudomorphic BiQuaRTT.	54
21.	Cross-section TEM of selectively etched (RIE) and regrown QuESTT structure.	57
22.	Cross-section TEM of selectively etched (thermal MBE) and regrown QuESTT structure.	59
23.	Simulation of the band structure and carrier density of a QuESTT type device that includes an InGaAs layer used as an etch stop.	62

FIRST ANNUAL INTERIM REPORT
CONTRACT NO. N00014-87-C-0363

SUMMARY

The historical trend of exponential improvement in cost and performance of integrated circuits can be traced primarily to downscaling of minimum geometries resulting from progress in design, lithography, and processing. However, due to the onset of fundamental limits, downscaling will cease to be an option for non-cryogenic operation in the mid-1990s, unless revolutionary devices and chip architectures are developed. Unipolar tunneling devices based on heterojunction technology appear to circumvent the scaling limits of conventional devices, and are therefore of interest as a potential solution to the device portion of this problem. A particular type of heterojunction device called a resonant tunneling transistor was selected for this effort.

In the following pages, results of the first year of research and development of resonant tunneling transistors are described. Unlike some devices that have been called "resonant tunneling transistors," which are really conventional devices incorporating resonant tunneling diode structures, these are "true" resonant tunneling transistors. A true resonant tunneling transistor consists of a single-well, double-barrier resonant tunneling diode structure to which a third terminal, directly contacting the quantum well, has been added. Two types of resonant tunneling transistors (RTT) are included within the scope of the contract: a unipolar version called the Quantum Excited-State Tunneling Transistor (QuESTT), and a pseudomorphic bipolar version called the Bipolar Quantum Resonant Tunneling Transistor (BiQuaRTT). A lattice-matched version of the BiQuaRTT has been developed at TI under an earlier Air Force contract. Although the bipolar devices do not meet the downscaling requirements, they require less difficult processing and can serve as a valuable proof of principle and guide to design of unipolar devices.

The report describes the development of a theory of resonant tunneling structures and its use to derive device models that have been used in the

design of device structures. It also describes the extensive process development that has been required to permit contacting the very thin (50 Å) quantum well base layers, and also to isolate the emitter, base, and collector layers. The processes developed have been used to fabricate transistors, and these devices have been characterized electrically. The characterization reveals that a pseudomorphic BiQuaRTT, which shows transistor action with a current gain of five, has been fabricated. Achievement of a functional QuESTT is thought to be imminent.

This report discusses plans for the immediate future in the modeling, process development, and device fabrication/characterization efforts, and concludes with recommendations for the remainder of the contract period.

I. INTRODUCTION

A. Need for Quantum Devices/Circuits

The downscaling of minimum geometries of transistor-based ICs will eventually be brought to an end by a combination of problems related to devices, interconnections, noise, and reliability. The resulting saturation of circuit densities almost certainly implies a saturation of the historical exponentially downward trend in cost and volume per bit or function, which has been a primary driving force for the increasing pervasiveness of electronics in DoD systems. Scaling has also provided exponential improvements in device speed and power dissipation, which have led to substantial enhancement of system performance. Because the introduction of sophisticated electronics into these systems has significantly improved their capabilities, it is appropriate to inquire whether an alternative scenario that significantly prolongs exponential trends in cost and performance exists.

Estimates based on abstract physical switching device models that are independent of specific device technologies indicate that several orders of magnitude in downscaling of device power in devices with minimum geometries of a few hundred angstroms would be theoretically permitted, if an appropriate non-transistor device technology could be found. The key to this search is to employ electronic phenomena that are characterized by dimensions much smaller than the depletion layer widths and diffusion lengths that provide the basis for conventional transistor function.

A step can be taken in this direction by using heterojunctions rather than p-n junctions to introduce potential barriers for purposes of carrier confinement. This approach is currently limited to GaAs, however, because of the absence of an adequate heterojunction technology for silicon. Nevertheless, as we shall see, this approach can be carried to the limit of completely unipolar devices employing only heterojunctions for confinement, totally eliminating all p-n junctions, and their associated space-consuming depletion layers, from the device.

The advent of MBE and similar technologies permits the fabrication of semiconductor heterostructures with features on the scale of nanometers. These capabilities have been applied to the development of semiconductor devices with significantly improved performance. Three distinct thrusts may be identified within this worldwide development effort. The first is to apply heterostructure technology to improve what are essentially classical semiconductor devices. The Selectively Doped Heterostructure Transistor (SDHT), which is also known as the High Electron Mobility Transistor (HEMT), and the Heterojunction Bipolar Transistor (HBT) are examples of this thrust. The second thrust is to employ heterostructures in optoelectronic devices, to exploit their ability to confine carriers and optical fields and to modify quantum states of electrons. The third thrust, which has had by far the smallest total effort of the three, is to find novel physical phenomena enabled by nano-scale heterostructures that can lead to truly revolutionary device mechanisms. Because semiconductor structures having dimensions comparable to the Bloch wavelength of electrons can be fabricated, the obvious place to look for such phenomena is in quantum-mechanical effects.

Quantum mechanical tunneling is an electron transport mechanism that becomes important when the thickness of potential barriers to carrier transport becomes very small, of order $0.01 \mu\text{m}$ (100 \AA). It is of interest because it potentially permits carrier transport control by electrical means in structures far too small to operate as conventional transistors. Three-terminal devices based on tunneling may thus provide a means of continuing the historical exponentially downward trend in minimum device geometries, and in switching power and delay, beyond the limits of transistors.¹

The progress of AlGaAs/GaAs heterojunction technology has rejuvenated interest in tunneling devices, and particularly in the use of quantum wells to modify the density of states available to tunneling carriers. The most popular structure for study has been the single quantum well, double-barrier resonant tunneling diode (RTD).^{2,3} Prior to the inception of this contract, TI and others had demonstrated resonant tunneling diodes (RTDs) with superior low-temperature negative differential resistance (NDR) characteristics,⁴ and TI had shown that NDR persists at high temperatures in these devices.⁵ NDR,

perhaps due to incoherent resonant tunneling, has also been shown to persist at frequencies as high as 2.5 THz.³

Early experience with Esaki diodes has shown, however, that although diodes exhibiting NDR can be used for switching, large scale integrated circuits based on such threshold logic devices are not realizable.⁶ Three-terminal devices that provide sufficient current gain for fanout are required, and the fabrication process must be suitable for integration.

B. Resonant Tunneling

Resonant tunneling structures are the simplest case of devices exhibiting quantum confinement and coupling. Confinement in these types of structures is achieved in one dimension by utilizing quantum well heterostructures. The first investigation of these structures was done by Chang, Esaki, and Tsu,² who observed weak structure in the current-voltage characteristics of resonant tunneling diodes at low temperatures. Interest in these structures was revived by the work of Sollner et al.³ A number of groups are now actively studying resonant-tunneling diodes and attempting to incorporate resonant-tunneling structures into three-terminal devices (transistors).

A typical resonant tunneling diode structure is shown in Figure 1. The most often used material is the lattice-matched GaAs/AlGaAs system, where the highly doped contacts and central quantum well are GaAs and the barriers are $\text{Al}_x\text{Ga}_{1-x}\text{As}$. The two $\text{Al}_x\text{Ga}_{1-x}\text{As}$ layers that define the central GaAs quantum well serve as partially transparent barriers to electron transport through the device. Resonant tunneling occurs when the bias voltage across the outer electrodes is such that one of the quantum well bound states is at the same energy as some occupied states in the cathode and some unoccupied states in the anode. Peaks in the electron transmission as a function of incident electron energy thus lead to peaks in the current vs voltage characteristic of the diode. The structure is an electrical analog of a Fabry-Perot resonator.

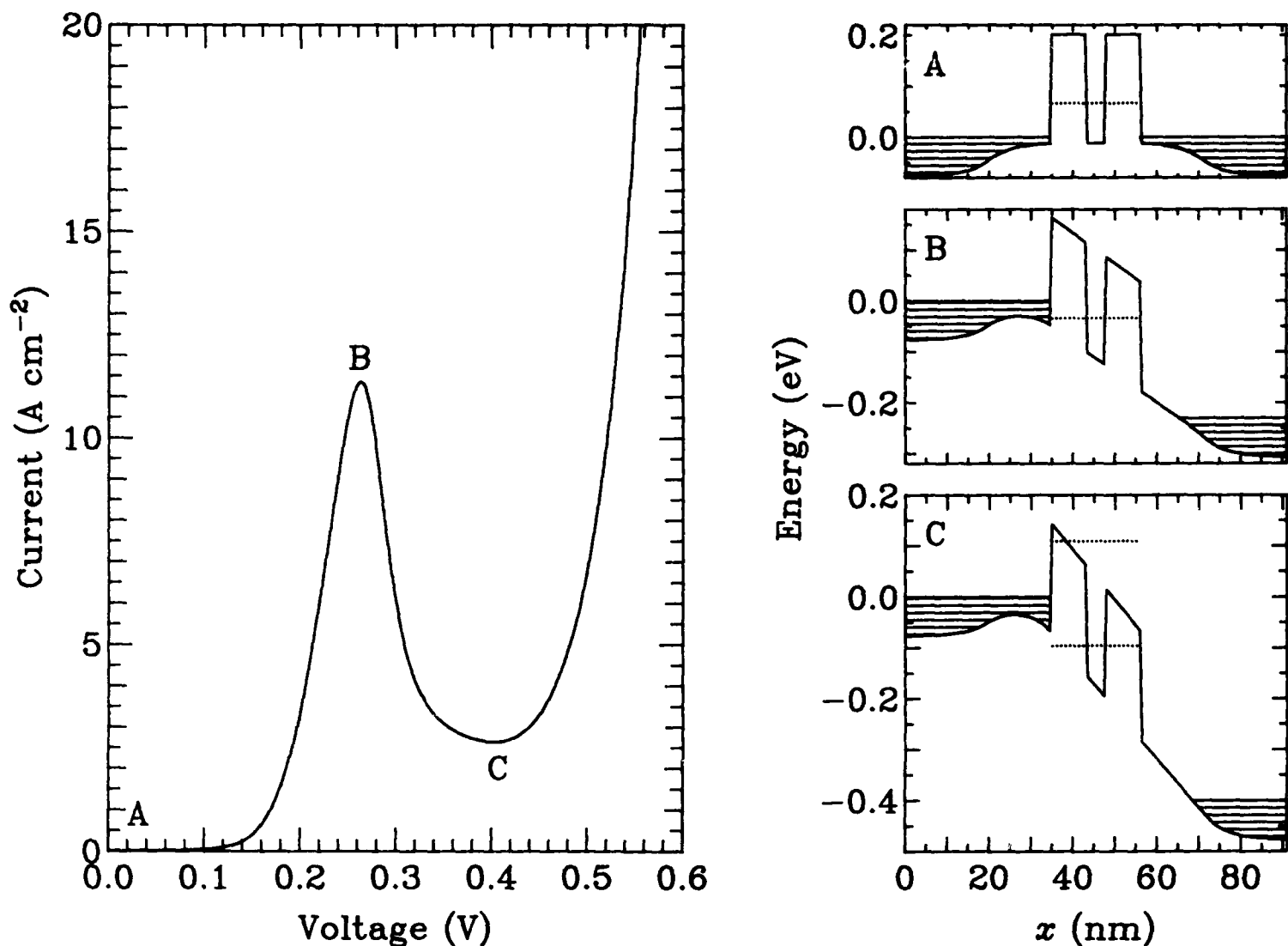


Figure 1. Characteristics and conduction-band profile of a resonant-tunneling diode. The $I(V)$ characteristic is plotted to the right. The points labeled A, B, and C correspond to the conduction-band profiles plotted to the right. The shaded areas of the band-profile plots show the occupied electron states and the dotted lines show the resonant energy levels. In equilibrium (A) there is no current flow. As the bias voltage is applied, the resonant level is pulled down so as to permit resonant tunneling (B), which appears as a peak in the $I(V)$ curve. The tunneling current then declines (C) as the resonant level is pulled below the conduction-band edge on the upstream side.

C. Resonant-Tunneling Transistors

1. Quantum-Classical Hybrid Devices

If one seeks to exploit resonant-tunneling in a three-terminal (transistor) device, there are, broadly, two different ways to approach this task. The simpler and presently more popular approach is to insert a resonant-tunneling quantum well structure into one electrode of an otherwise conventional device. Examples of this approach employ bipolar,⁷ hot-electron,⁸ and various field-effect⁹ transistors. The perceived advantages of such structures lie in their novel $I(V)$ characteristics, typically including a negative resistance region and leading to multistable states in simple circuits. The problem with this approach is that the same characteristics would be more easily obtained by simply connecting a negative-resistance resonant-tunneling diode in series with the conventional device. To illustrate this, we have fabricated such a device in the simplest possible way: by wiring together a resonant-tunneling diode with an off-the-shelf transistor. The $I(V)$ characteristic of such a hybrid is shown in Figure 2. The hybrid device consists of a series combination of a normal MOSFET and a double-barrier resonant tunneling structure and exhibits the characteristics that most series combinations do: negative differential resistance, negative transconductance, etc.

There is thus no persuasive reason for intimately integrating the transistor and the resonant-tunneling diode; they could just as well be fabricated side-by-side on the same chip. The more promising approach is to build what we describe as a "true" tunneling transistor, in which the structure is designed so that the quantum well is independently contacted and its potential may be adjusted independently of the adjacent electrodes. This will permit a full exploitation of the tunneling transport mechanism, and is the approach of the present program.

2. True RTTs

The goal of the present program is to demonstrate three-terminal quantum semiconductor devices of each of two designs that will be described below. They are referred to by the acronyms QuESTT (for QUantum Excited-State Tunneling Transistor) and BiQuaRTT (Bipolar QUantum Resonant-Tunneling Transistor). These devices were conceived within the constraint that



Figure 2. I(V) characteristic of a series combination of a RTD and MOSFET. The MOSFET is at room temperature, the RTD at 77 K.

nanometer resolution should only be required in the vertical direction, which is readily achieved using epitaxial growth techniques. Because quantum-mechanical effects are permitted in only one spatial dimension, the present devices are closely analogous to the purely classical bipolar and hot-electron transistors. However, the obvious approach of simply scaling down a classical device to quantum dimensions¹⁰ leads to fundamental problems that require a modification of the device design. The analysis of these problems and the rationale behind the QuESTT and BiQuaRTT designs is described below.

To make a three-terminal quantum device, one needs a way to control the current through the device with a voltage or current supplied to the control electrode. The current through the device may be presumed to be conducted by resonant tunneling of electrons. The obvious approach should be to try to manipulate the potential of the quantum well. If this is to be done through the electrostatic potential, then mobile charges must be added to or removed from the structure by the control electrode to act as sources of the perturbation in the potential. It is in the nature and behavior of these charges that the fundamental problems lie.

In semiconductors, the available charge carriers are electrons and holes. In view of the recent successes of ballistic hot-electron devices,^{11,12} let us first consider what happens when we try to use electrons to control the tunneling current. The problem with such schemes is that the "cold" electrons in the base are still quantum-mechanical particles and they have to occupy allowed quantum states in the quantum well. The lowest state is typically the state through which the current-carrying electrons are supposed to tunnel. Thus it is difficult to maintain the distinction between the controlling and current-carrying electrons in this structure. Another way to view this problem, as illustrated in Figure 3, is that the base-collector barrier is not sufficient to confine the electrons in the base if it is thin enough to permit resonant tunneling. This leads to an excessive base-collector leakage current of sufficient magnitude to completely short out the base and make transistor action impossible. Devices of this structure have been built and show precisely this behavior.¹³

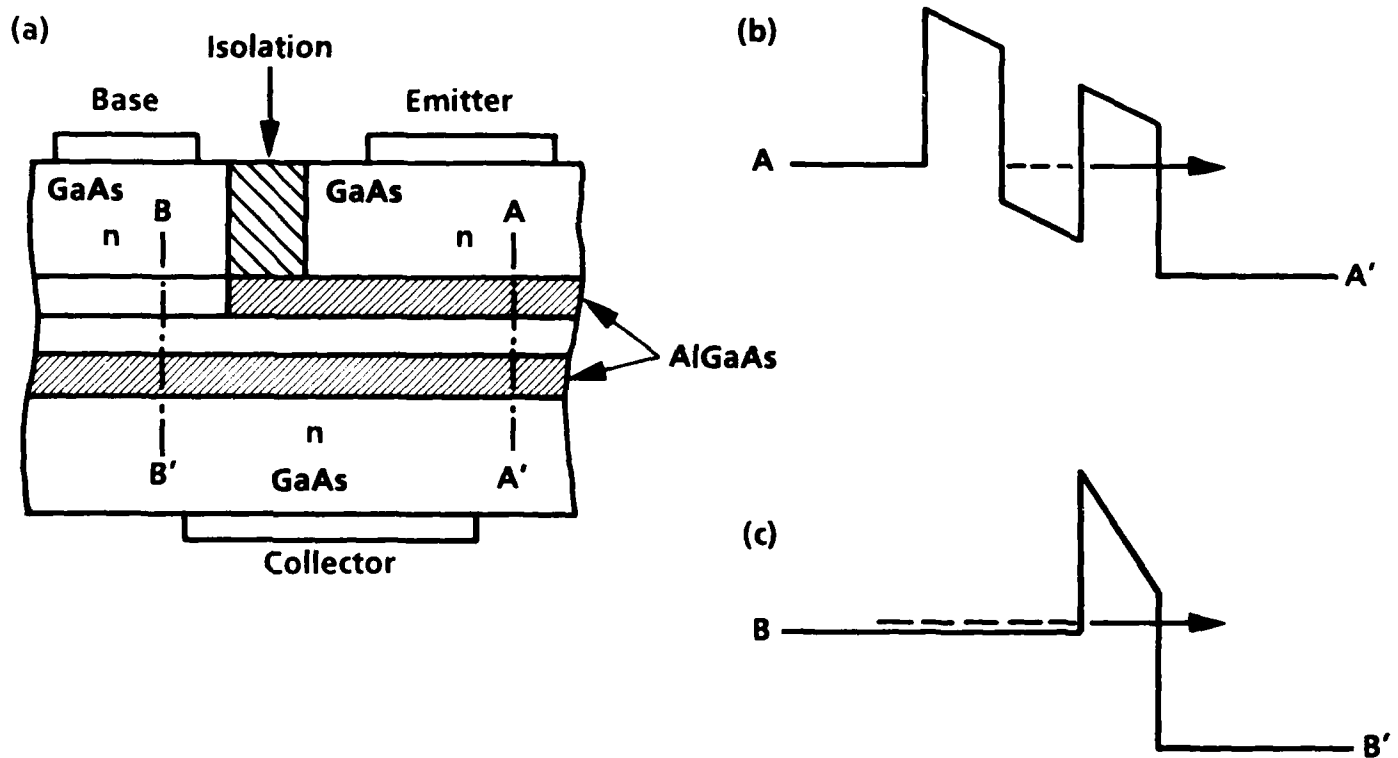


Figure 3. (a) Hot-Electron Tunneling Transistor. (b) The band diagram through AA' shows tunneling behavior, but (c) that through BB' shows parasitic base current.

To overcome this problem, a device called the QUantum Excited-State Tunneling Transistor (QuESTT) was invented at Texas Instruments. This structure uses a narrower-bandgap quantum well layer to "hide" the lowest-lying electron state from the tunneling electrons, thus making it available to the control electrons, as shown in Figure 4. The control electrons are injected into and removed from the base by a tunneling contact to a thick layer of the narrow-bandgap material. This device thus requires a selective epitaxial regrowth process to make the base contact.

As with the unipolar device described above, the most obvious bipolar quantum transistor structure will not work. The problem becomes apparent if we consider the energy-band diagram of the resonant-tunneling structure. Such a band diagram is shown in Figure 5. To achieve resonant tunneling, the potential of the bottom of the quantum well must be biased below the bottom of the conduction band in the source electrode. Notice what this implies about the emitter-base bias: it must be greater than the narrower bandgap, and in the forward direction for current flow. Now we have to have some way to make contact to the holes in the quantum well, and this implies a bulk region that is doped p-type. If this p region is in contact with the n-type emitter, a catastrophic current will result.

The solution to this problem is the same that led to the QuESTT. The quantum well can be made of a narrower-bandgap material, which will reduce the bias voltage required to turn on the device to a manageable level. We will refer to this device as the Bipolar QUANTum Resonant Tunneling Transistor (BiQuaRTT). The band diagram of the resulting structure is shown in Figure 6. The contact to the base of this device can be achieved with conventional fabrication technology, using either ion implantation or diffusion of acceptors. The compositional disorder resulting from either of these processes is actually of benefit because it helps to reduce the energy barrier between the contact and the base layer.

In view of the known band alignments at GaAs-based heterojunctions, a practical BiQuaRTT design will usually involve tunneling through the second state in the well, leaving the ground state vacant for control carriers. However, there is still the problem of catastrophic leakage currents. Since

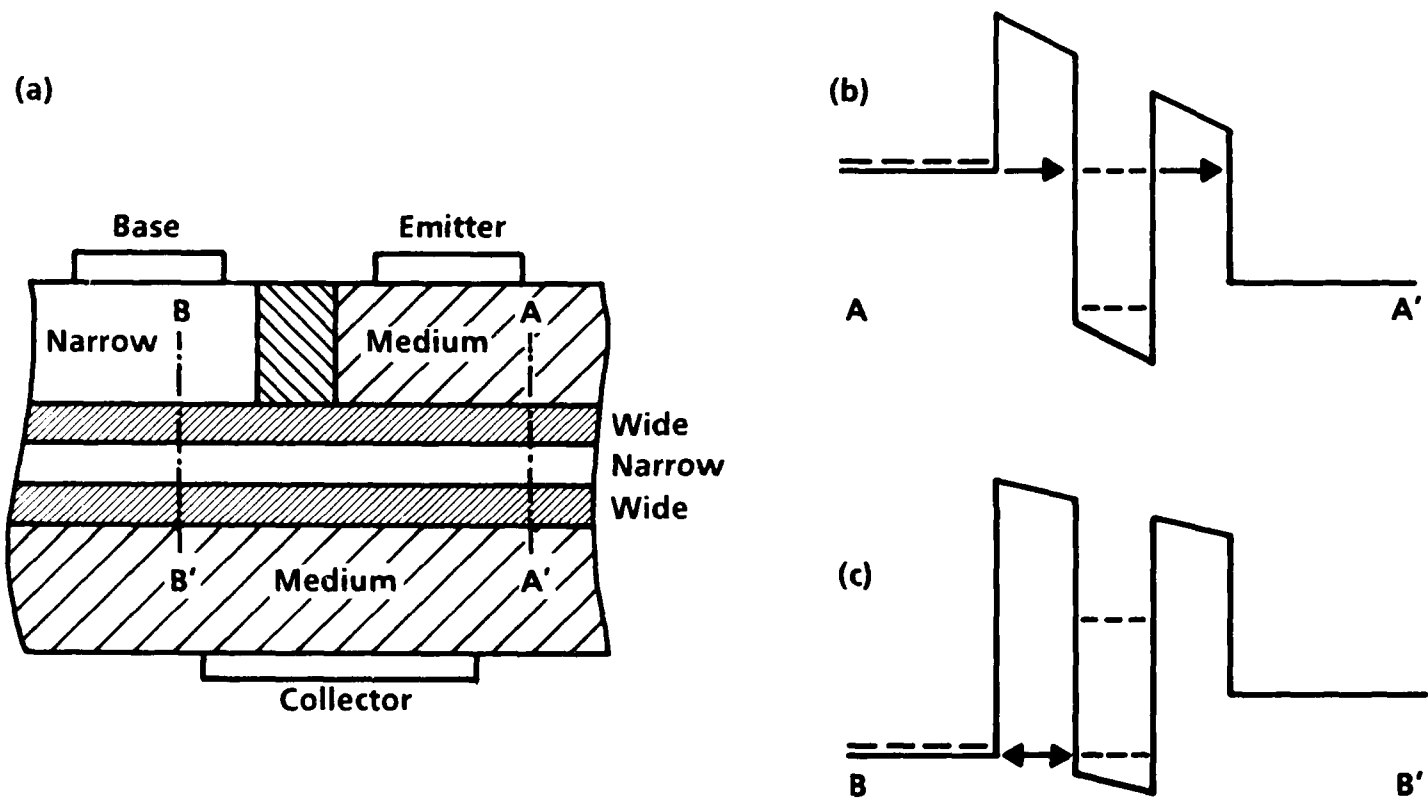


Figure 4. (a) Quantum Excited-State Tunneling Transistor. (b) Shows collector current derived from tunneling through the excited (upper) quantum-well state. (c) Control carriers supplied to the ground state by the base contact and confined by the medium-gap collector.

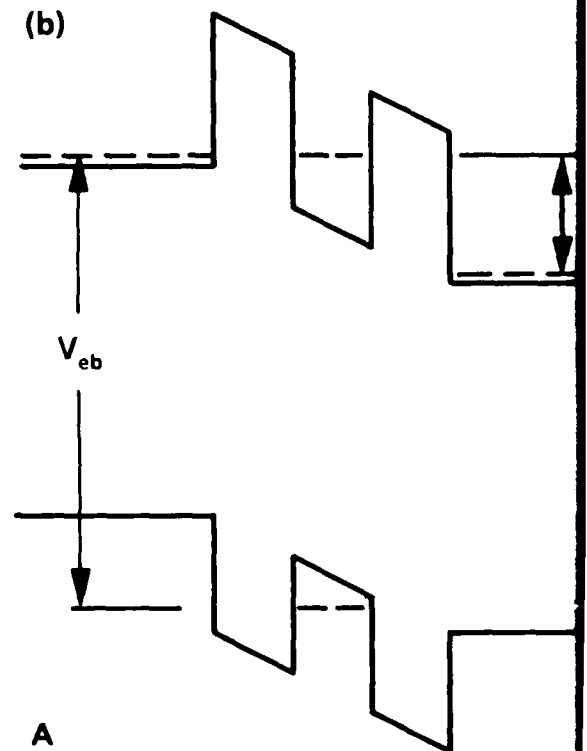
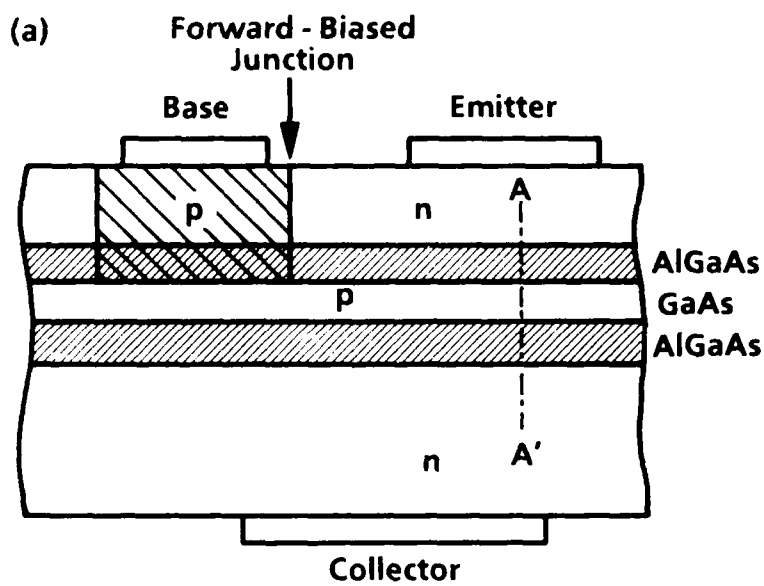
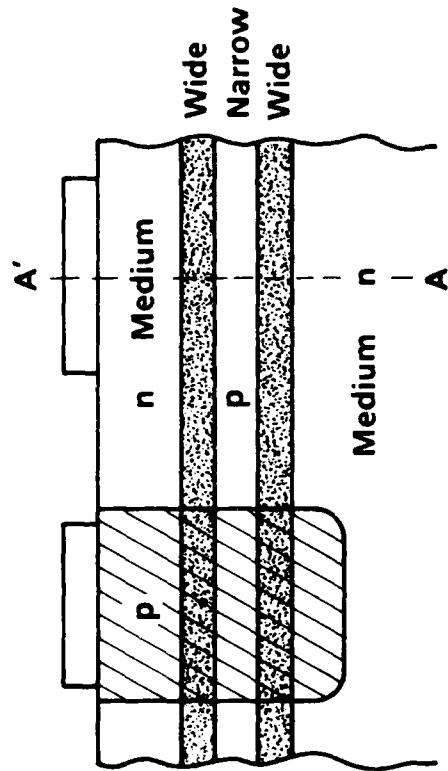
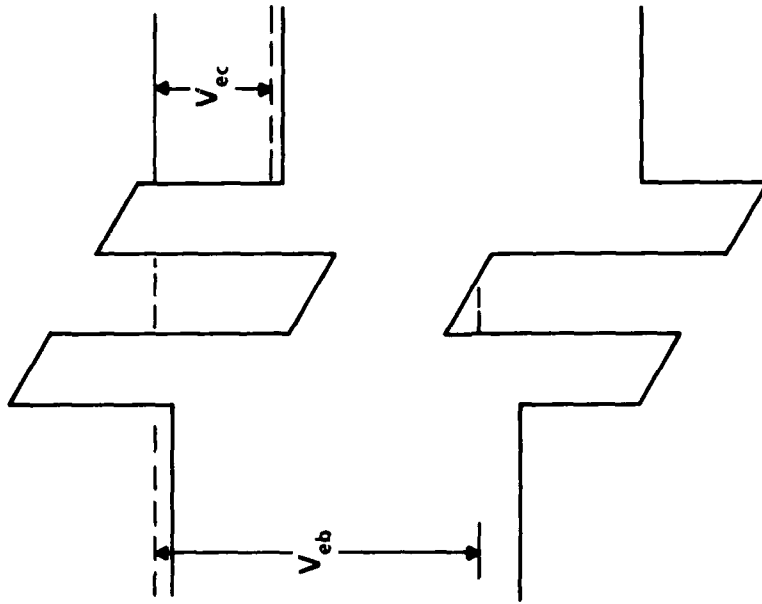


Figure 5 (a) Bipolar Tunneling Transistor. The energy band diagram through Section AA' shown in (b) illustrates the problem of the forward bias required for this device to operate.



(a)



(b)

Figure 6 (a) Bipolar Quantum Resonant Tunneling Transistor. The energy band diagram through Section AA' shown in (b) illustrates the reduced forward bias voltage due to the narrow-bandgap quantum well.

the ground state is not actively involved in the tunneling, it can be "hidden" below the conduction band.¹⁴

A number of options exist for the creation of wider-bandgap regions in the emitter and collector (with respect to the quantum well). One option is to utilize an $\text{Al}_x\text{Ga}_{1-x}\text{As}$ emitter/ $\text{Al}_y\text{Ga}_{1-y}\text{As}$ tunnel barrier/ $\text{Al}_z\text{Ga}_{1-z}\text{As}$ quantum well structure ($y > x > z > = 0$). Another is to utilize multi-material systems, such as a GaAs emitter/ $\text{Al}_x\text{Ga}_{1-x}\text{As}$ tunnel barrier/ $\text{In}_y\text{Ga}_{1-y}\text{As}$ quantum well structure, as previously mentioned. A third option is to create a wider-bandgap material in the emitter/collector by using superlattices; i.e., a $(\text{GaAs}/\text{Al}_x\text{Ga}_{1-x}\text{As})$ superlattice emitter/ $\text{Al}_y\text{Ga}_{1-y}\text{As}$ tunnel barrier/GaAs quantum well structure.

However, the structure cannot be designed indiscriminately since the screening of the quantum well by the n^+ cladding layers can deplete the well. This implies that (a) the well may have to be doped to unrealistically high levels, or (b) the doping in the collector/emitter regions must be physically moved further away. One quickly realizes then that the structure need not be symmetric, since the current density through the structure is determined by the emitter source contact. Progress on this variation will be outlined in a further section.

II. PROGRESS/PLANS

A. Device Theory

The theoretical tasks within the present program are directed toward two different objectives. The first is to support the experimental development of the BiQuaRTT and QuESTT by providing usable models that relate the structural design of the device to its electrical properties. The second is to advance the fundamental understanding of the physics of tunneling in semiconductor heterostructures to provide the scientific basis for further progress on nanoelectronic devices. The primary approach to both of these objectives is to use numerical techniques to simulate, at a number of different levels of sophistication, the behavior of the device structures.

1. Device Models

The key to understanding and designing any heterostructure device is the energy-band profile of that device. (That is, the energy of the band edges as a function of position.) When one considers how such a device might operate, or how it might fail to operate, it is necessary to consider the band profile. When one designs a device, what one specifies are the epitaxial layer thicknesses and doping levels. This should produce the desired band profile under the applied voltage bias. To assure that this is the case, one must have a way to compute the band profile given the layer sequence and the applied voltages. The programs that fall under the heading of "device models" perform this function.

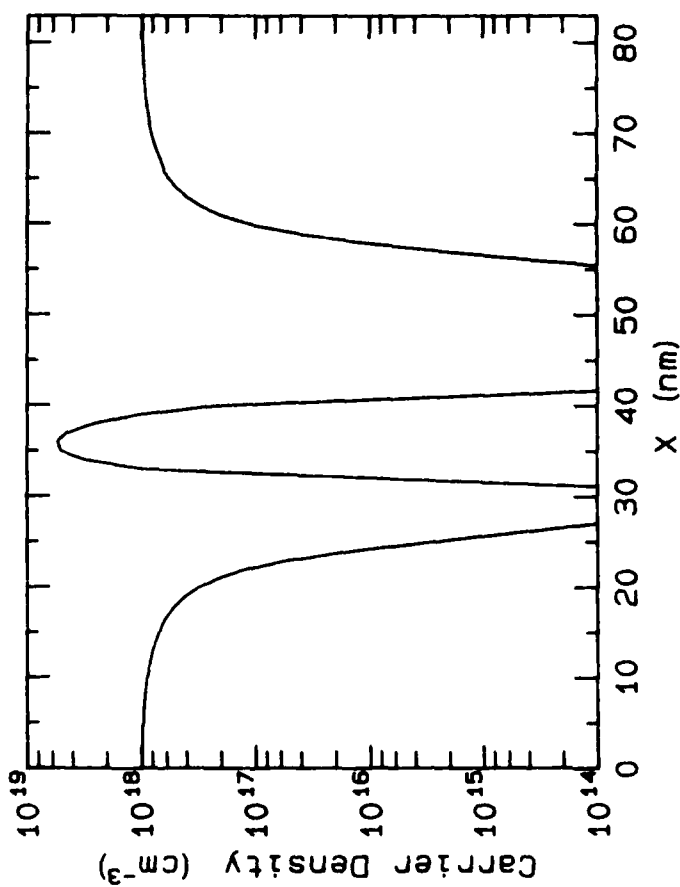
A computer code that models the BiQuaRTT structure was developed prior to the start of the present program. During the program it was modified to model the QuESTT. Both of these codes have been released to Advanced Concepts branch staff members who are concerned with device design and fabrication. This has proven to be a very effective approach to the distribution of theoretical results. Because these codes are run by the engineers designing the device, the appropriate structures are simulated, and the answers to the detailed questions that arise in the course of device design are answered. We have observed that the device engineers tend to run a much larger number of cases than a computer modeling specialist is inclined to do, because the device people are cognizant of the detailed questions,

whereas the modeler is generally aware of only the broader questions that can be answered by modeling.

These program codes solve the self-consistent Fermi-screening problem. That is, they assume that in the contact layers of the device (meaning everything outside the quantum well) the electron density is simply given by the Fermi distribution function. The quantized states in the quantum well are found by solving Schrödinger's equation and the occupation of these states is derived from the assumption that those carriers are in equilibrium with the base electrode. The resulting charge distribution is evaluated self-consistently with Poisson's equation for the electrostatic potential by a conventional Newton iterative algorithm. The program that models the BiQuaRTT is named BIQMODEL and the output from a typical run of this code is shown in Figure 7. The energies of the resonant states are found by evaluating the quantum-mechanical transmission coefficient from a finite-difference approximation to the Schrödinger equation and searching for peaks in the transmission.

A new computer code, QUESTTMOD, was developed during the course of the program to implement a Fermi-screening model of the QuESTT. It is similar in function and usage to BIQMODEL. An example of the output of QUESTTMOD is shown in Figure 8.

During the development of QUESTTMOD it became obvious that better software engineering practices should be applied to the family of programs that includes QUESTTMOD, BIQMODEL, and some other programs for modeling resonant-tunneling diode structures. These practices consist primarily of consolidating code that performs identical functions in different programs into a common file that is included into each of the separate programs by a compiler directive. This makes corrected or upgraded code immediately available to all of the programs using that common code file. The implementation of this practice required some effort to resolve differences in the approaches or semantics of the different programs. The process of code consolidation has been completed.



T = 77 K 10 DEC 1987 10:25

Thickness	Composition	Doping
25 nm	Al _{0.35} Ga _{0.65} AS	N 1.0x10 ¹⁸ cm ⁻³
5 nm	Al _{0.35} Ga _{0.65} AS	Intrinsic
3 nm	ALAS	Intrinsic
8 nm	GaAS	P 6.0x10 ¹⁶ cm ⁻³
3 nm	ALAS	Intrinsic
5 nm	Al _{0.35} Ga _{0.65} AS	Intrinsic
35 nm	Al _{0.35} Ga _{0.65} AS	N 1.0x10 ¹⁸ cm ⁻³

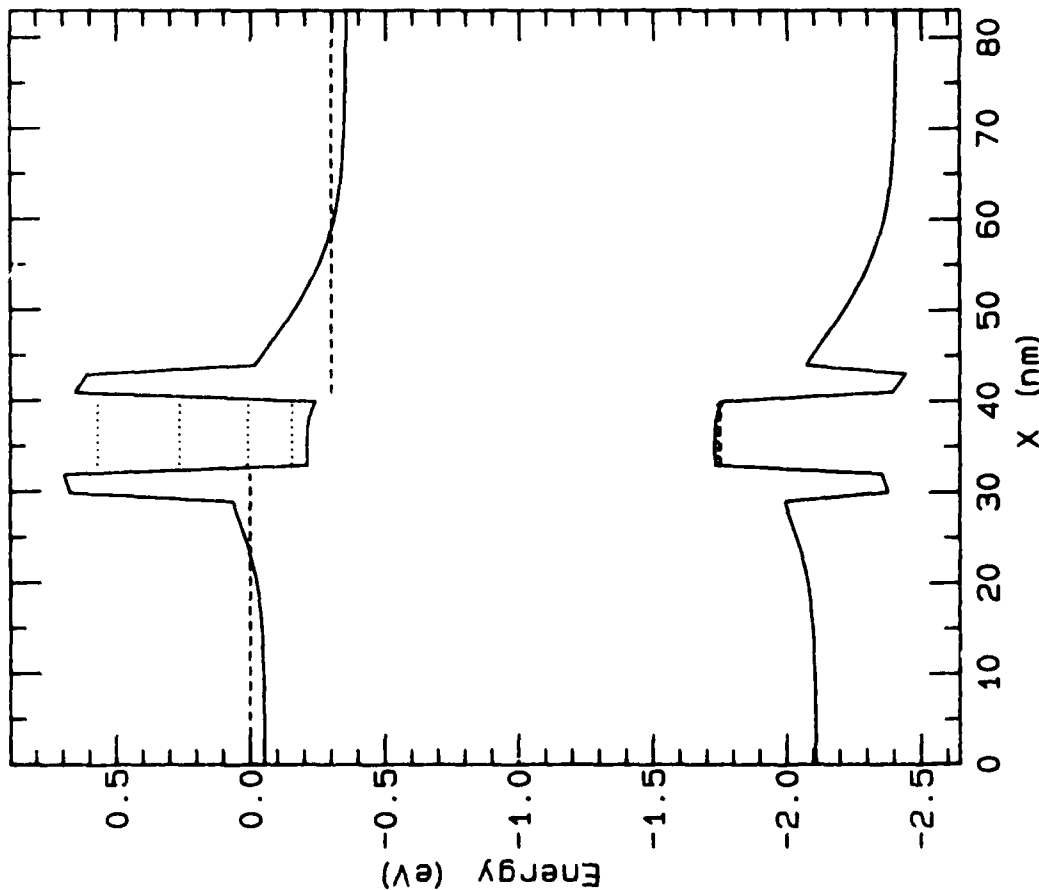


Figure 7. Results of a typical run of the BiQuaRTT modeling program BIQMODEL.

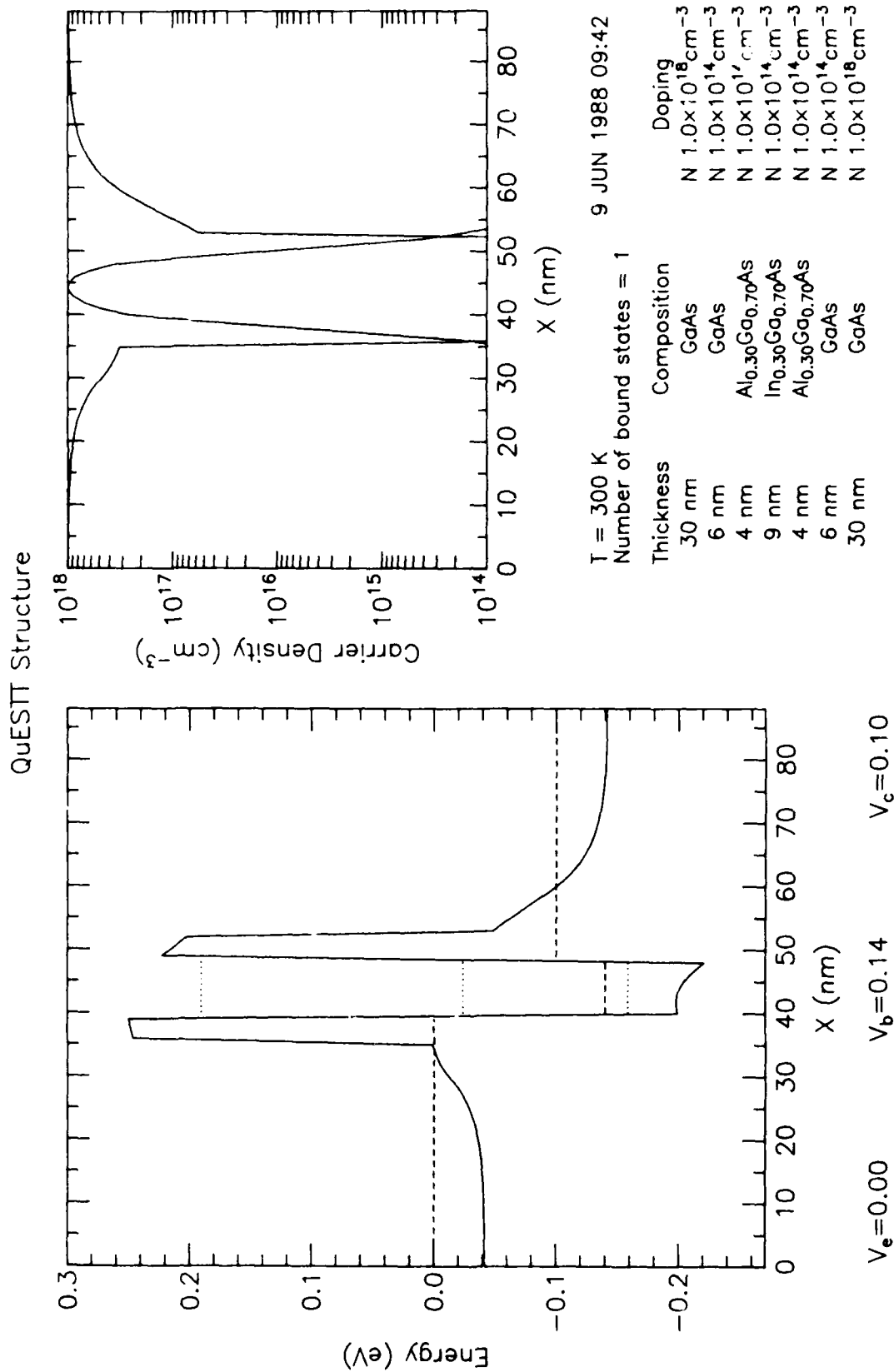


Figure 6. Output of QuESTTMOD. The plot to the left shows the conduction-band energy as a function of position through the structure. The Fermi levels of the three terminals are shown as dashed lines, and the quantum well state energies are shown as dotted lines. The plot to the right shows the carrier densities as functions of position, and the text below this plot documents the structure and parameters of this run.

The consolidation of the program code that implements the Fermi-screening self-consistency and stationary scattering state calculations has permitted us to systematically incorporate improved algorithms into these programs. Several aspects of the calculations were significantly improved. Some subtle modifications were made into the way that the effective-mass discontinuity is modeled in the finite-difference solution of Schrödinger's equation. This has improved the agreement between resonant energies calculated with this method and those evaluated analytically, so that the difference is now less than one milli-electron-volt for a typical structure. We also implemented a better algorithm for integrating over the transmission coefficients to obtain the total current. We had previously used a rather "brute force" numerical integration algorithm with a fixed step size. The new code recursively refines the step size, and chooses an appropriate approximating form for the transmission coefficient curve (Lorentzian near a resonance; polynomial elsewhere). This code runs in a much shorter time than the previous routine. We have also configured the code so that different distribution functions for the electron sources, representing structures of different dimensionality, may be employed in evaluating the current. This was done to investigate the effects of lateral confinement on the $I(V)$ curve of a resonant-tunneling structure, and the results are shown in Figure 9.

We also developed a vastly improved Fermi-screening solution technique. The new technique simplifies the Newton iteration scheme for solving the coupled nonlinear equations derived from this model, and employs the Bank-Rose damping scheme to stabilize and optimize each step of the Newton iteration. The Bank-Rose scheme works for problems that can be derived from a variational principle and it chooses the scalar coefficient of each Newton step to minimize the functional, which appears in the variational formulation. This technique has been implemented in program code that solves the Fermi-screening problem for the resonant-tunneling diode (neglecting any electrons in the quantum well). The resulting program executes about one order of magnitude faster than the previous approach. We plan to incorporate this improved technique into the QUESTTMOD and BIQMODEL programs (which necessarily include charge in the quantum well) in the near future.

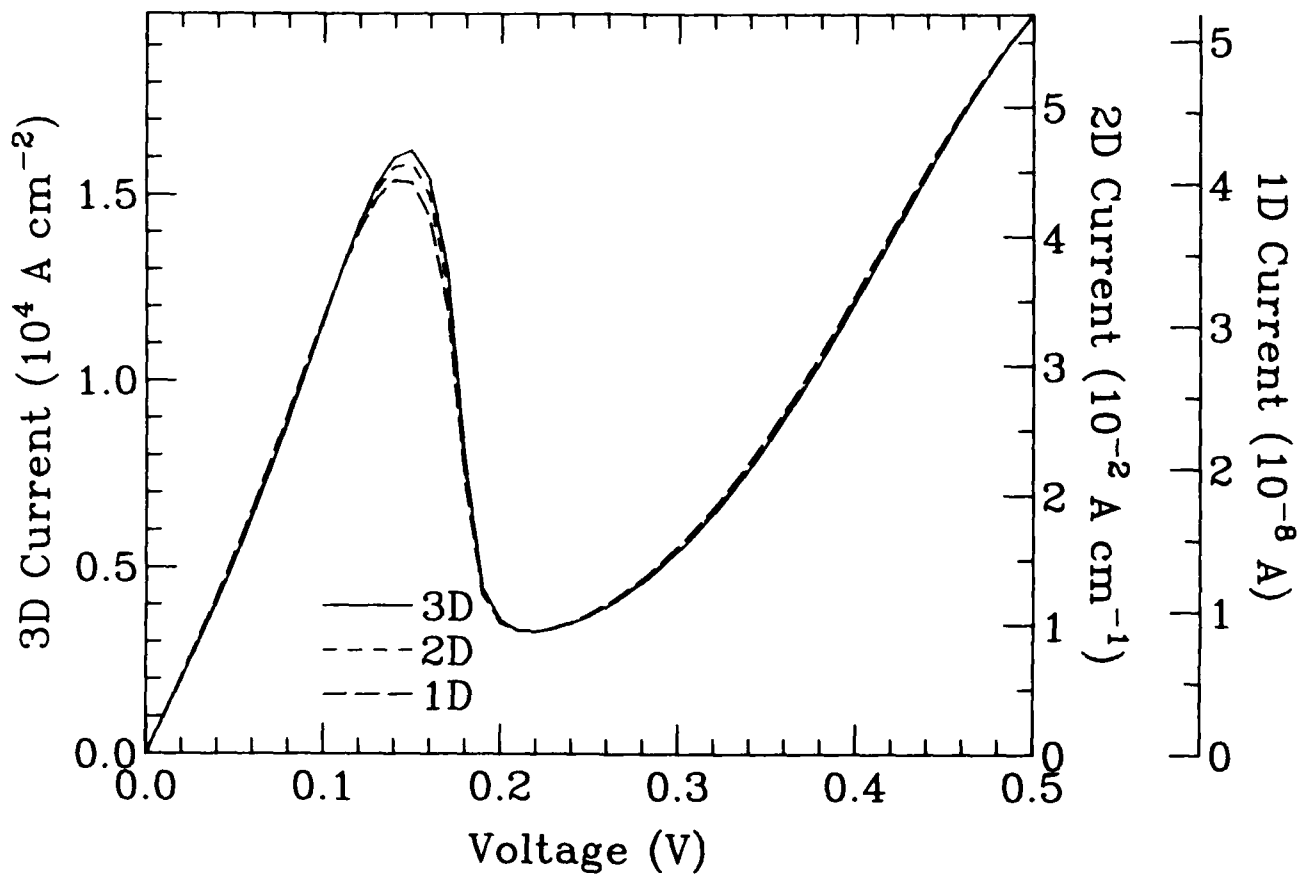


Figure 9. Scattering-theory $I(V)$ curves for laterally-confined structures. Curves are shown for a large-area resonant-tunneling diode (labeled "3D"), one in which the electrons are confined in one lateral dimension (labeled "2D") and one in which the electrons are confined in both lateral dimensions (labeled "1D"). It appears that lateral confinement will not significantly effect the peak-to-valley current ratio.

2. Physics of Tunneling Heterostructures

An adequate exploration of the physics of tunneling in semiconductors requires a broad array of theoretical techniques. We have employed three general techniques to investigate issues of particular importance to the overall understanding of quantum transistor physics. These include two approaches based upon the Schrödinger equation: wavepacket calculations and scattering-state calculations. A quantum transport theory based upon the evaluation of an open-system Wigner distribution function has been employed to investigate time-irreversible phenomena.

a. Wavepacket Calculations

We have performed calculations in which the time-dependent Schrödinger equation is integrated to observe the evolution of a wave function and to test the more abstract estimates of the characteristic tunneling time. Most of these estimates invoke the width (in energy) of the resonance peak in the transmission coefficient. To obtain the detailed time-dependent wave function, we have developed a computer code that calculates directly from the time-dependent Schrödinger equation the time evolution of an initially specified electron wave function. A key aspect of this algorithm is that it preserves the fundamental unitarity requirement (preservation of normalization) on the time-dependent wave function to extremely high precision. This is implemented through a Crank-Nicholson finite difference scheme. We intend to use this program to address several questions pertaining to the lifetime of an electron in a double-barrier resonant tunneling structure. In particular, we plan to compare the results of our direct microscopic calculation to the more ad hoc estimates of resonant state lifetimes obtained from standard transmission coefficient calculations.

Shown in Figure 10 is the time-dependent probability (absolute magnitude squared of the wave function) of finding an electron in a double-barrier quantum well, as obtained from our program. The location of the double-barrier structure is also shown for reference and is plotted in arbitrary units. The system here is of 2000 Å total length, and consists of two 225 meV barriers of 24 Å width with the quantum well being 50 Å wide. An effective electron mass appropriate to GaAs was used throughout. The initial

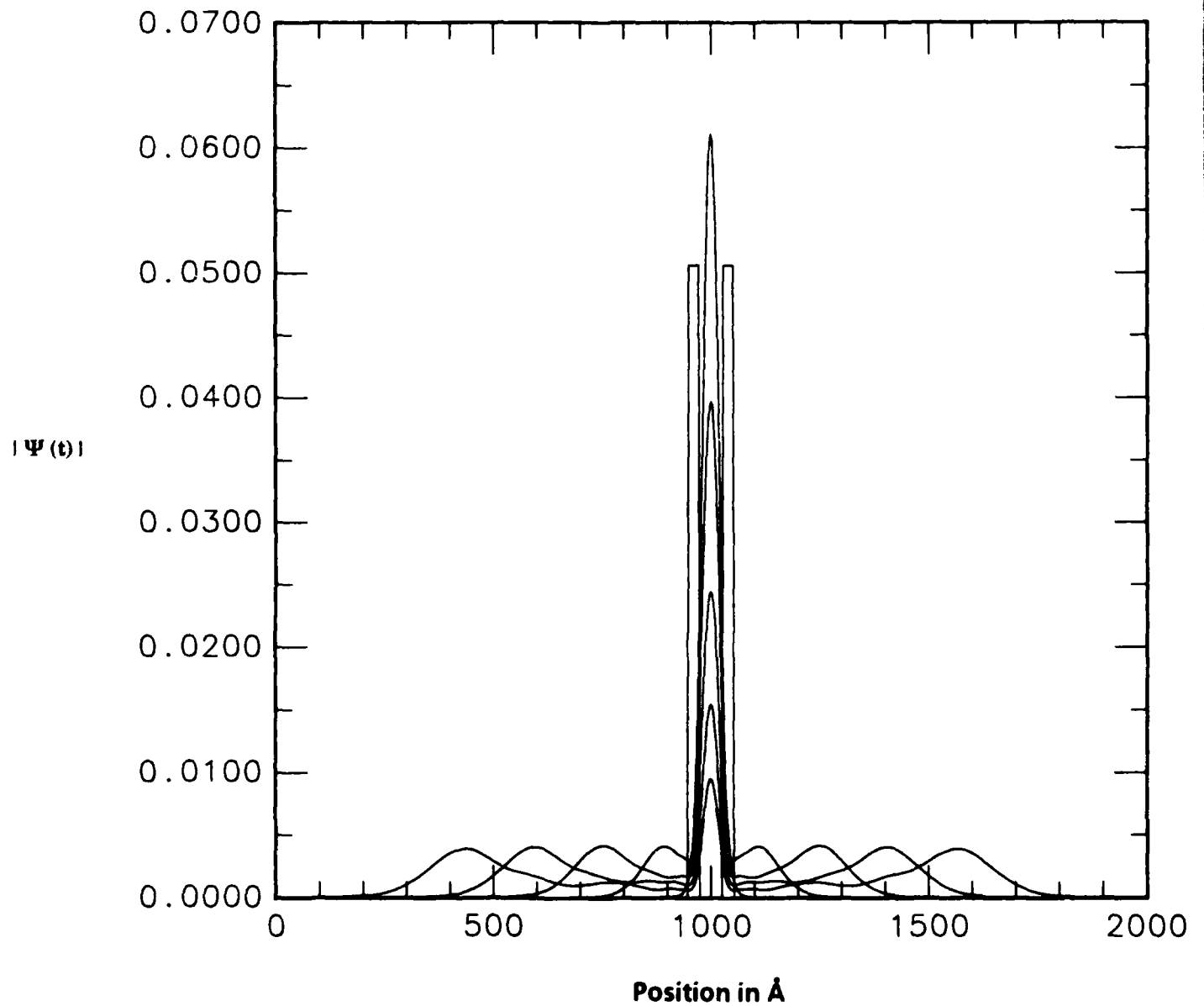


Figure 10. Time evolution of an electron wavepacket escaping from a quantum well by tunneling.

state is for an electron localized to the quantum well, and has an energy of 71 meV. The subsequent drop in probability in the center of the well is clearly seen as the electron leaks out of the well via tunneling. Once outside the well, there is a clear front to the wave function that indicates a freely propagating particle. Note that there is also diffusive broadening in the width of the wave function as time proceeds. A snapshot of the wave function has been given at every 36 fs.

Shown in Figure 11(a) is the decay in time of the probability of finding an electron in the quantum well of an idealized (flat-band) symmetric double-barrier structure, given that the electron was placed there initially with an energy close to the tunneling resonance. The results of Figure 11(a) have been obtained from a direct numerical integration of Schrödinger's equation, starting from a suitably chosen wave function localized in the quantum well. Data are shown for three barrier widths of 51 Å, 59 Å, and 68 Å, corresponding to the solid, dashed, and dotted lines respectively, with the well width held fixed at 54 Å in all three cases. Parameters representative of GaAs-AlGaAs systems have been employed. Note that the electron escapes fastest for the thinnest barrier, as would be expected. The dependence of the tunneling rate upon barrier width is discussed below. The initial wave function has been selected as an eigenstate of an isolated quantum well with the same width and depth as the well in the double-barrier structure. The bound-state eigenvalues of the single well form a good approximation to the resonant tunneling levels of the corresponding double-barrier system for energies not too near the top of the well. From Figure 11(a), the electron probability decays with an overall exponential time dependence, with some small oscillations superimposed. These oscillations are believed to be the result of the small admixture of some higher-lying state into the initial condition.

The inverse of the decay rate defined by the slope of the line in Figure 11(a) forms a simple characterization of an electron's lifetime in a double-barrier quantum well. In Figure 11(b) are shown (solid lines) the lifetime results obtained from a least-squares analysis of time-dependent probability data, such as in Figure 11(a), for 18 barrier widths between 50 Å and 100 Å, with the well width held fixed. The dashed lines are discussed

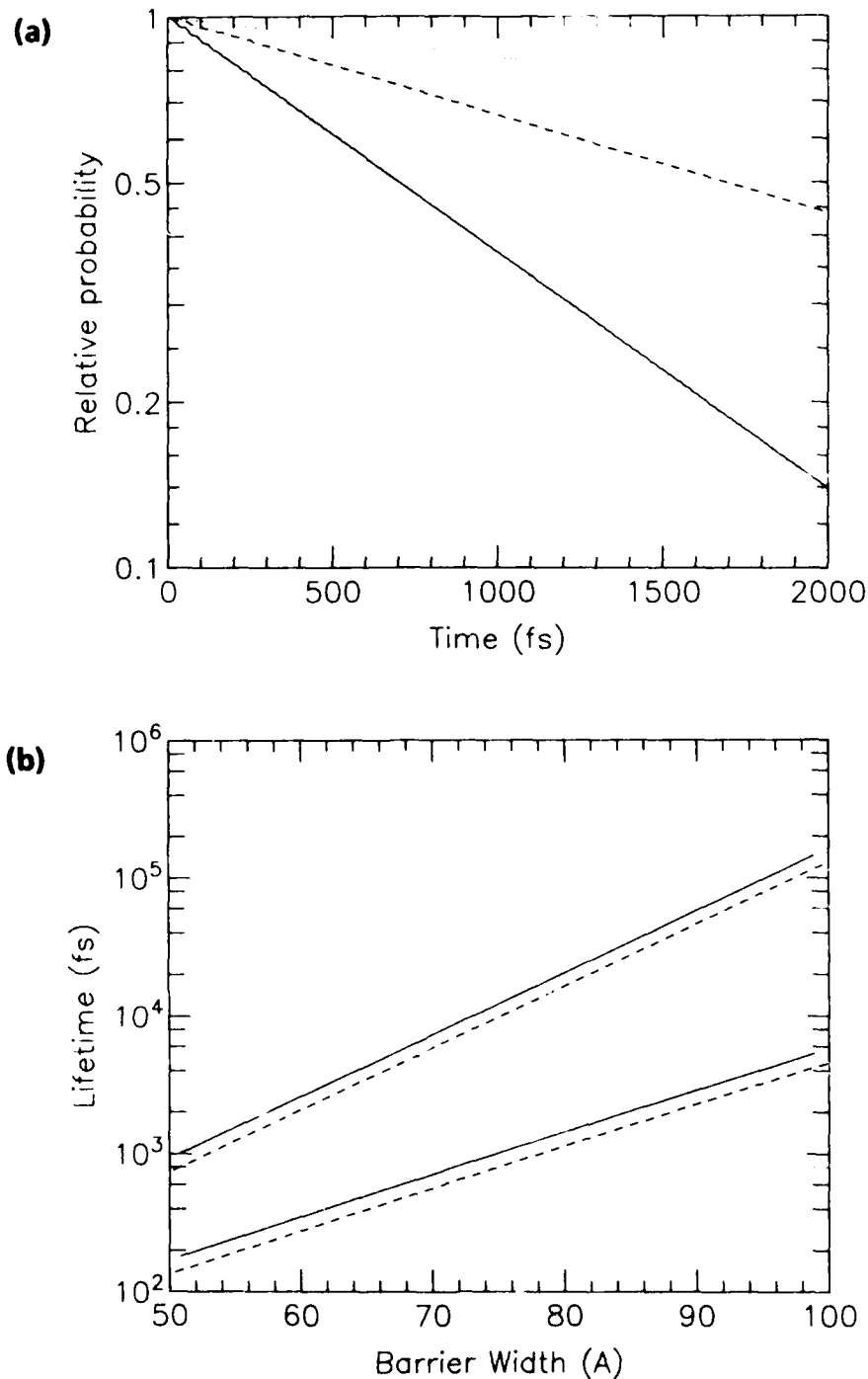


Figure 11. Results of a simulation of the escape of a wavepacket from a quantum well. (a) Shows the time-dependent decay of an electron's probability of being found in the quantum well of a double-barrier structure, given that it was there at time zero. The results for several barrier thicknesses are shown, with the well width and electron energy held fixed. (b) Shows the lifetime for escape versus barrier thickness. The upper curves are for an electron placed in the ground state while the lower curves are for an electron placed in the first excited state. Solid lines are from time-dependent Schrödinger equation. Dashed lines show the scattering theory time delay.

below. The two solid lines correspond to quantum well widths of 82 Å (lower) and 54 Å (upper), respectively. The lower solid line was obtained from the tunneling escape of an electron placed in an excited level of the quantum well as the initial state, while the upper was derived from a ground state. The excited state has a higher tunneling probability, and thus it yields a generally smaller lifetime (for fixed barrier width), in agreement with the results in Figure 11(b). It is readily seen that the lifetime increases exponentially with barrier width. The difference in slope between the two solid lines in Figure 11(b) is attributable to the difference in the resonant tunneling energy levels between the lowest and first excited tunneling levels for the two wells considered.

The dashed lines in Figure 11(b) are from a widely used estimate of the lifetime of a resonant tunneling state, which we can compare with the results of our calculation for the escape lifetime. If one assumes the transmission coefficient to have a Lorentzian shape near a tunneling resonance, then under this assumption the time delay of steady-state scattering of incident plane waves is given by the width of the transmission coefficient at resonance divided by the reduced Planck constant. We have taken this width to be the full width at half-maximum (FWHM). This is also the lifetime estimate one would obtain by invoking the uncertainty principle. It is commonly asserted in the literature that the scattering time delay is equal to the quantum mechanical tunneling time through double-barrier structures. We find from our calculation that the lifetime for escape of an electron suddenly created in a quantum well is approximately 25% longer than the scattering time delay. The latter, of course, refers to the delay across the scattering region of plane waves, which are infinite in extent. The disparity between these two measures of the lifetime in a double-barrier resonant tunneling system, although not significant for the purposes of ballpark estimates, points out the importance of initial conditions in defining a relevant time. One must specify the process one is interested in to obtain meaningful times. Simply put, there is not a single time scale to characterize the response of a double-barrier structure. To further explore the role of initial conditions, and recognizing that electrons come in wavepackets of finite extent, we have used our time-dependent Schrödinger

equation code to study the transmission times of wavepackets at the resonant energy incident upon a double-barrier structure.

Figure 12 shows the time development of the probability of finding an electron in the quantum well, given that a Gaussian wavepacket with a mean wave-vector corresponding to the resonant energy tunnels through the system. The system chosen has a well width of 82 Å, barrier widths of 51 Å, and a barrier height of 225 meV, as do all of the systems reported here. The parameters considered for Figure 12 correspond to the system with the smallest lifetime shown in Figure 11(b). The mean energy is such that the wavepacket tunnels through an excited state of the double-barrier system at 158 meV. The effective mass of GaAs was used uniformly throughout the system. There are three curves shown in Figure 12. The solid line is for a wavepacket with a momentum spread in the Fourier components comprising itself, which corresponds to the energy width (FWHM) of the transmission coefficient at the tunneling resonance.

The dashed line is for a momentum uncertainty corresponding to twice the FWHM in the transmission coefficient, while the dotted line is for a momentum spread half the FWHM. Thus, as we go from the dashed to the solid to the dotted lines in Figure 12, we have progressively more wave-vector components in the wavepacket, which are near the tunneling resonance. In real space, the wavepacket becomes progressively broader as the momentum uncertainty becomes smaller. We see in Figure 12 that as we get more "on" the resonance, the longer it takes to build up the resonant state amplitude in the well. Note that the time involved for the build-up process is of the order of thousands of femtoseconds. This measure of the lifetime of the electron in the well is clearly an order of magnitude larger than the times indicated in Figure 11(b) (for the same system parameters). It is interesting to note that while the "rise time" characteristics of the build-up of probability in the well are determined by the initial condition, the decay of probability is universal, as indicated by the curves being parallel for later times in Figure 12. This decay time differs from those in Figure 11(b). For the system considered in Figure 12, one would have from Figure 11(b) a decay time of approximately 150 fs, while the universal decay time in Figure 12 is of order 350 fs. It is not surprising that the decay time from

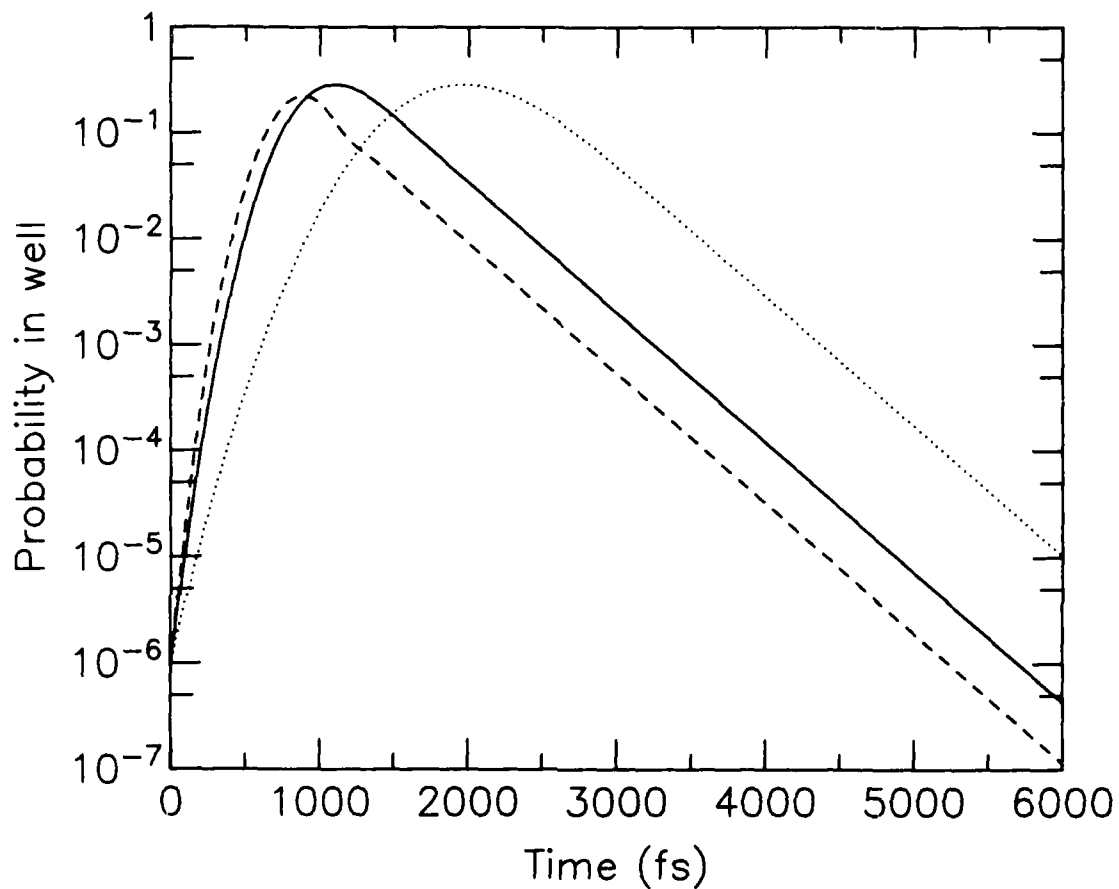


Figure 12. Results of a simulation of the transmission of a wavepacket through a quantum well. The curves plot the total probability for the electron to be in the quantum well as functions of time. The different curves correspond to incident wavepackets with different widths. The rate of initial build-up of the probability increases as the spatial width of the packet decreases. The rate of decay of the probability is independent of the initial condition.

Figure 12 does not agree with the time delay shown in Figure 11(b), since the latter is tied to the behavior of a plane wave of a single Fourier component exactly on the resonance. The momentum uncertainty is zero here, which corresponds to an electron wave infinite in spatial extent. Such a wave continuously populates the quantum well at the resonant amplitude and thus the decay time of Figure 12 is not obtained in this type of steady-state theory.

b. Quantum Transport Theory

We have continued to elaborate the quantum transport theory of tunneling devices, based upon evaluation of the Wigner distribution function, that was originally developed at Texas Instruments under Contract No. N00014-84-C-0125, "Research on GaAs Quantum-Coupled Structures That Can Be Used as Electron Devices." Because this approach is based upon quantum statistical mechanics, rather than pure-state quantum mechanics, it is able to handle irreversible phenomena such as phonon scattering in a much more complete fashion than the more widely practiced approaches. This has allowed us to identify and investigate a critical issue: How do inelastic scattering processes affect the self-consistent electrostatic potential in a resonant-tunneling diode and in particular how accurate is the screening picture employed in the device models described above?

The simple screening picture assumes that there is a high rate of inelastic processes in the contacting layers. This is required to enforce the local equilibrium condition and in particular to create the electron accumulation layer on the upstream side of the tunneling structure. If such processes are not operative, the qualitative features of the band profile are not immediately apparent.

Investigation of this question required development of a program code that would implement self-consistency of the electrostatic potential. Whereas the nonself-consistent model is cast as a set of linear equations that are easily solved by direct calculation, the coupling to Poisson's equation introduces a nonlinearity into the model. This means that an iterative algorithm must be used to solve the equations. We implemented a multidimensional Newton iteration scheme, of the sort commonly employed in classical semiconductor device modeling. In this scheme, the nonlinear

equations are rewritten as a (large) vector of functions such that the equations are satisfied when the functions are all equal to zero. The zero of the vector of functions is found by repeated moves in a "downhill" direction, as determined by the solution of a Jacobian equation. One of the tricky issues in such a calculation is the determination of the optimum distance to move in a given step. The Bank-Rose damping scheme described above gives a good answer to this question for equations that may be derived from a variational principle (such as equilibrium or quasi-equilibrium problems). However, transport equations are necessarily time-irreversible and are therefore not obtainable from a simple variational principle--thus the Bank-Rose scheme does not apply to the steady-state problem for the self-consistent Wigner function. We have therefore developed an empirical (numerical) damping scheme that works well for all of the cases we have tested. It leads to convergence in about thirty iterations in most cases. The Jacobian of the nonlinear problem has about twice as many nonzero elements as the Liouville super-operator of the linear problem, which means that it takes four times as much CPU time to perform one iteration of the self-consistent calculation as it takes to solve a linear case. Thus a four-minute solution of the nonself-consistent case requires eight hours when self-consistency is implemented.

The results of the self-consistent Wigner function calculations demonstrate the issue identified above: The nature and strength of the inelastic scattering processes in a resonant-tunneling device have a profound effect on the shape of the self-consistent potential. This is illustrated in Figure 13, which compares the potential and electron density profiles obtained under various assumptions about inelastic scattering. If such scattering is neglected entirely, the solution obtained in Figure 13(a) is obtained. This does not at all resemble the profile that we would expect based upon a static screening theory. Instead of an upstream accumulation layer and downstream depletion layer dropping the applied voltage, almost all of the voltage is dropped in an upstream depletion layer. A consequence of this profile is that the electric field, rather than approaching zero at the boundary, has a large value at the boundary. This clearly unphysical sort of solution has also been obtained by others.¹⁵ The key point is that to obtain the behavior that we conventionally call screening, inelastic processes must

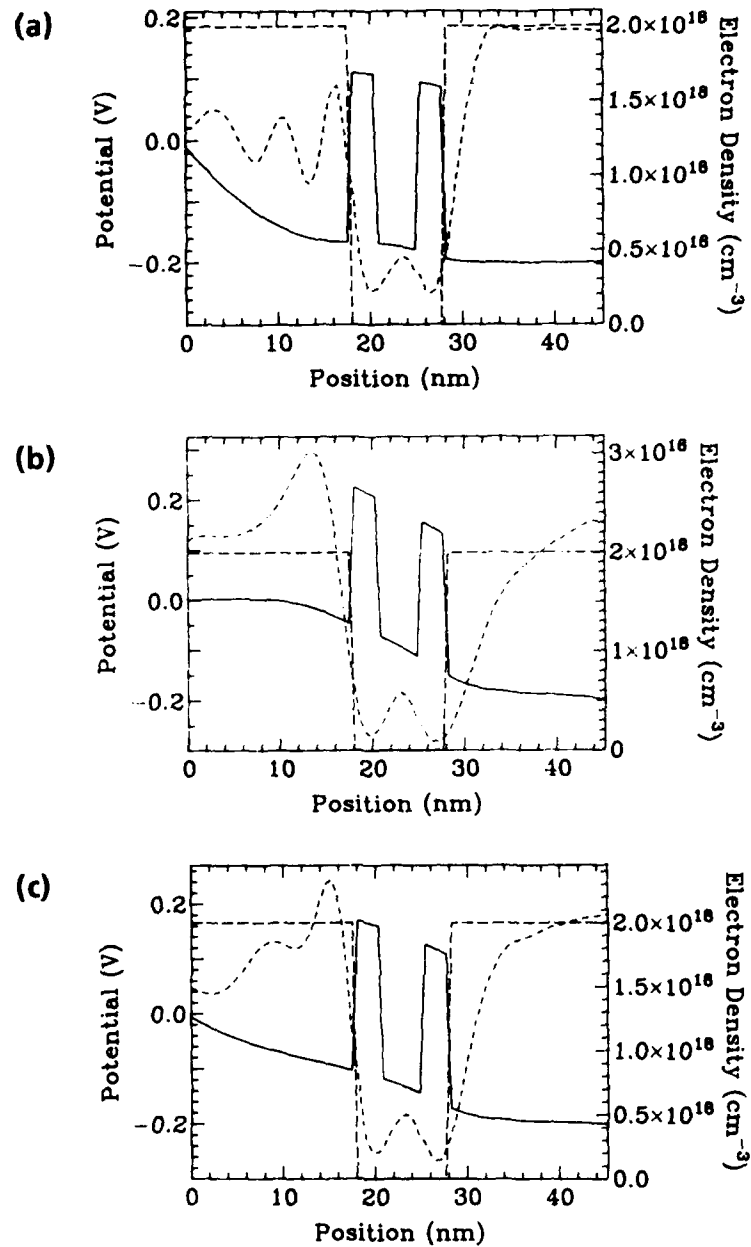


Figure 13.

Self-consistent simulations of a resonant-tunneling diode using the Wigner distribution. In all of these plots the potential profile is shown by the solid line, the electron density is shown by the short-dashed line, and the doping profile (on the same scale as electron density) is shown by the long-dashed line. (a) Shows a simulation with no relaxation included. Note that the voltage is almost completely dropped to the left of the barrier, and that the electric field at the left boundary is unphysically large. (b) Shows a calculation in which a relaxation term with a 40 fs relaxation time was included. The resulting potential profile is much more like that we expect based upon screening theory. (c) Shows a calculation in which realistic scattering rates for LO and acoustic phonons in GaAs are included. These do not provide enough scattering to support the screening picture.

be present. This is because screening occurs when mobile carriers such as electrons accumulate in regions of lower potential, and to accumulate, they must lose kinetic energy through inelastic processes. This effect is illustrated in Figure 1(b), which shows a simulation in which a relaxation term has been included. The potential profile is much more like that obtained from screening theory. However, the relaxation time used for this simulation was 40 fs, which corresponds to a mobility of $1000 \text{ cm}^2/\text{Vs}$, too low for GaAs. A more realistic calculation is shown in Figure 1(c), in which the actual Fermi-golden-rule scattering rates for longitudinal optical (LO) and acoustic phonons were included. It is apparent that these processes do not provide sufficient dissipation to validate the screening picture.

We would expect that a device with insufficient dissipation to approach the static screening picture would have an electric field extending over a greater than expected distance. This would lead to an excess voltage drop that might be interpreted as an excess series resistance in experimental devices. To determine whether such effects occur in our devices, a set of samples with well-characterized structure and varying barrier thicknesses have been fabricated and are presently being measured.

The self-consistent results, which show a large electric field at the boundary, suggest that perhaps the boundary conditions themselves should be reexamined. The present simulations fix the electrostatic potential at the boundaries and fix the distribution of incoming electrons. Physically, if an electric field extended into the sample beyond the boundary of the simulation domain but still within the semiconductor material, we would expect that the peak of the electron distribution will shift in response to that field (making, to lowest order, a displaced Maxwellian distribution). In other words, the incoming distribution would be responsive to the self-consistent potential. Such a feature is not contained in the present calculations. It has been included in some simulations by Mains and Haddad,¹⁶ with promising results. At this point the correct way to formulate the response of the ohmic-contact boundary conditions is not at all clear. We plan to investigate this issue by comparing different models of the contact phenomena.

As mentioned above, the self-consistent Wigner-function calculations are computationally intensive, and this is at present a major barrier to the progress of this work. To provide more computational power, we plan to run these simulations on a new Convex mini-supercomputer recently installed in the VLSI Design Laboratory. This will require the translation of our present program code from Pascal--as the version that we have used only runs on VAX machines--into C, which is a much more portable language. (To be more precise, the features that are required to support a large body of software such as our modeling code are not standardized in Pascal, whereas they are in C. Also a vectorizing Pascal compiler is not yet available.) We have at present translated and tested about half of the required lines of code.

The Newton iteration code provides the machinery by which other nonlinear effects in transport problems may be attacked. Chief among these are the effects of electron-electron scattering and Pauli exclusion. We would recommend that these effects be initially investigated in a purely classical model of a hot-electron transistor. The program code that we are using to evaluate the Wigner function can be readily adapted to solving the classical Boltzmann equation, simply by replacing the nonlocal potential operator (which is required to describe quantum interference) with a local (classical) force term. This would provide a self-consistent model of the hot-electron transistor in which all of the important effects are included, and that will require considerably less computational resources than the popular Monte Carlo approaches. It would also provide a basis for a comparison of the potential performance of the QuESTT versus the classical hot-electron transistor.

c. Scattering-State Calculations

The calculation of stationary scattering states is the most popular approach to the theory of tunneling phenomena, and has largely shaped conventional intuition concerning such phenomena. By stationary scattering states, we mean solutions to the time-independent Schrödinger equation that are asymptotically free states and are thus unnormalizable. (Note that in this context "scattering" refers to the coherent scattering of the wave function from the device structure, not to random scattering from phonons or

impurities.) Such calculations are usually implemented as evaluations of the transmission matrix. We have preferred to use a purely numerical finite-difference approach to the solution of Schrödinger's equation. This has the advantage that it can handle arbitrarily shaped potentials, and incorporate such realistic details as discontinuities in the effective mass and nonparabolicity of the energy-band structure. We have used the computer codes that implement these calculations for a variety of purposes, including evaluating the current density through QuESTT and BiQuaRTT structures and as a standard of comparison for the Wigner-function calculations.

In the course of the present program we discovered that there was a programming error in the evaluation of the current density. We had intended to implement the correct kinematic factor pointed out by Coon and Liu,¹⁷ but an error in the coding effectively implemented the incorrect (and more commonly employed) factor. Let us briefly describe the difference: The current carried by a state is proportional to nv where n is the density and v is the velocity. Now for a scattering state of a given energy E , the probability of it getting through the quantum well and thus contributing to the current is $|T|^2$, where T is the transmission coefficient. However, this is the probability that it will appear on the outgoing side, thus it should be multiplied by the velocity on the outgoing side. This is a critical distinction in a biased device, because the potentials on the two sides of the structure are different, and thus the velocities of a particle of energy E are different. It is commonly assumed, mistakenly, that the correct velocity is that on the incoming side, and this mistake is reinforced by the fact that it leads to analytically elegant expressions because the velocity factor cancels with the "density of states" factor in an expression for the current density. In fact, these factors do not cancel, and the resulting contribution has a large impact on the predicted valley current in a resonant-tunneling diode.

The result of correcting this error is that the $I(V)$ curves obtained from the corrected scattering calculation are in much better agreement with the Wigner-function calculations. The new comparison is shown in Figure 14. There is still a disagreement in the vicinity of the valley current, but even here the disagreement (expressed as the ratio of the

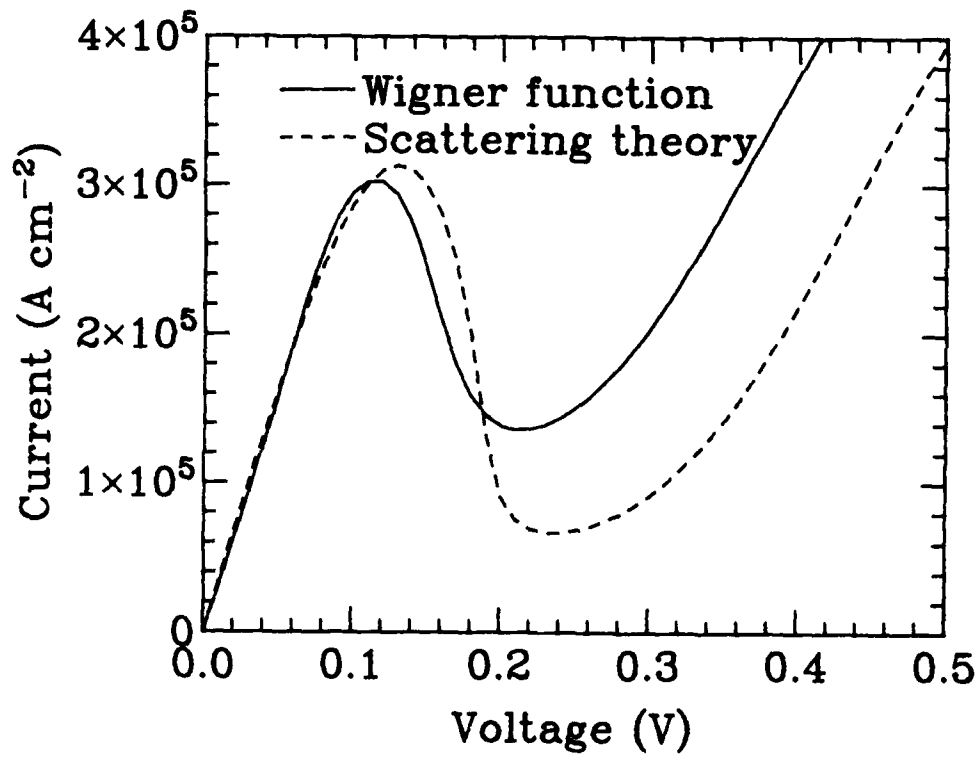


Figure 14. Comparison of the I(V) curves obtained from the Wigner-function and scattering theory calculations. The corrected scattering theory results are in much better agreement with the Wigner function results than those obtained earlier.

currents from the two techniques) is much smaller than we previously thought. In fact, the peak-to-valley ratio predicted by the scattering calculations now comes quite close to experimentally observed values, and preliminary calculations of the $I(V)$ curve at 77 K show an improvement in the peak-to-valley ratio of a magnitude similar to that observed in good devices. This points toward the conclusion that phonon scattering has a rather small effect on the magnitudes of the peak and valley current, which agrees with what we had earlier obtained from models that incorporated phonon scattering into the Wigner-function calculations. (We still believe, as described above, that phonon scattering has a significant effect upon the shape of the potential and therefore upon the voltage at which the peak occurs.)

Our realization of the potential pitfalls of the apparently straightforward calculation of tunneling currents from stationary scattering states has led us to undertake a critical reexamination of this approach. Such a reexamination is also timely in view of the recent publication of contradictory results in this area. Coon and Liu¹⁷ found that the left- and right-incident states at a given energy are not orthogonal, which leads to an additional term in the expression for the current density to assure compliance with the Pauli exclusion principle. This conclusion has been disputed by Krivan, Kluksdahl, and Ferry¹⁸ who assert that the states are orthonormal based upon an argument that invokes the Lippmann-Schwinger equation.

Our results are in general agreement with those of Coon and Liu.¹⁷ We find that, if there is a net potential drop from one side of the device to another, the left- and right-incident states are not in fact orthogonal. We also find in such a case that states normalized such that the incident wave has unit amplitude are not normalized in the conventional sense. All of these results have been verified by comparison with the numerically evaluated wave functions. We have also identified a test case whose analysis will expose a number of possible errors in the calculation of tunneling current. This is the case of a device whose contacts are doped at different levels, but that is in equilibrium. In such a device the Fermi levels must be equal on both sides of the quantum well, but the kinetic energies at the Fermi levels will differ and thus there will be a potential

difference across the device. In equilibrium, however, detailed balance must hold, and this provides non-trivial constraints on the current density that will involve the nonorthogonal and unconventionally normalized states. A complete discussion of the results of this investigation will be presented in a future report.

B. Device Development

1. Process Development

There is a good deal of commonality in the QuESTT and BiQuaRTT device structures that we have attempted to exploit in developing process strategies that may be applied to both devices. A common mask set has been designed for the development of both QuESTT and BiQuaRTT discrete devices. This section will discuss the mask set and the processing approaches being explored. The differences in processing between the QuESTT and BiQuaRTT structures will be identified when appropriate. The mask set is necessarily flexible to permit investigations and variations on both baseline structures. The processing approach has evolved over the course of the year and will certainly continue to do so. Discussion of the device epitaxial structures appears in the following section on device development.

a. General Processing And Design Constraints

Much of the fabrication work accomplished to date used a mask set designed prior to the start of this contract. Based on experience with this older mask set, the new mask design has been improved to minimize processing difficulties and add new test structures. Similar to the previous set, this mask was designed to produce discrete devices that have not been optimized for any single application. Eighteen different discrete devices are included on each die. The principle variations are in emitter size and base-to-emitter spacing. Three of the transistors employ circular, rather than rectangular, geometries. The first operational BiQuaRTT devices produced under this contract used the new mask set.

In designing these devices, conservative design rules were employed. No features smaller than 2 μm were included. The most demanding placement accuracy required is $\pm 0.5 \mu\text{m}$, while most of the devices require

no better than $\pm 1.0 \mu\text{m}$. While the contact alignment tools available in our laboratory are capable of considerably better performance than these figures, these design rules will result in the high-yield device process necessary at this stage of the material and device development.

b. Contact To Well (Base)

The operating principles of both the QuESTT and BiQuaRTT require control of the potential of the quantum well to modulate the energy of the quantum states and thereby the tunneling current through the device. Even after ohmic contact is made to the quantum well (base), in both types of devices, the resistance of the quantum well is a significant concern. The well is very thin (typically on the order of 100 \AA) and often will be heavily doped, which will degrade mobility. A charge build-up in the well due to the resonant tunneling carriers may also perturb the base contact under operating conditions.

To provide the minimum distance from the low-resistance base contact to the tunneling areas of the device, the base contact was designed as an annulus that surrounds the emitter contact. This topology requires that a metal lead to the emitter contact cross over the base contact region. Although this arrangement has problems, we feel that minimizing base resistance is a more significant issue. The spacings between the emitter and base contacts have been varied across the device matrix.

Although several methods are being pursued, the best method of contacting the p-doped BiQuaRTT well, to date, has proven to be a p^+ implant. A separate mask level is used to define an ohmic metal layer to contact the implanted region. Furnace annealing has been used to form this contact, while rapid thermal techniques are being investigated.

For the QuESTT we had assumed that a selective etch down to the well and regrowth of a low bandgap material would be necessary to get good contact to the well and reasonable isolation from base to emitter. We are exploring two different types of etch and regrowth techniques, which will be discussed below. We also believe that an implanted contact to the well

might work for the QuESTT. In any of these cases the same mask set will support the fabrication development.

c. Emitter Contact

The emitter contact for both device types is simply an n-ohmic contact to a degenerately doped n-type layer. We have used a wide range of emitter sizes in our different devices. The emitters are square, ranging from 3 μm on a side to 30 μm . Measurements on large test structures demonstrate good quality ohmic contacts.

d. Collector Contact

The collector layer is below the quantum well. The emitter layer and quantum well structure must be etched away before the collector contact metal may be applied. With the previous mask set the same pattern was used for both etching and metal deposition. While this may be an acceptable process, it is possible for some of the metal to be deposited on the sidewalls of the etch trench, which would provide a short between the emitter and collector. We have therefore employed separate mask levels for collector etching and collector contact where the contact metal layer fits easily inside the etched region, thereby avoiding the possibility of the aforementioned short.

The collector contact region is adjacent to three sides of the base annulus. The one side is left open to permit metal runs to contact the base and emitter without crossing the collector trench and metal contact.

The collector contacts are made of heavily n-doped GaAs and use the same type of metallization as in the emitter contacts. Again we have measured good quality ohmic contacts.

e. Base-Emitter Isolation

An etch region between the emitter and base contacts (therefore an annulus) is used to electrically decouple these two regions. Figure 15 is a SEM of a device with emitter, base, and collector contacts formed and an isolation trench etched.

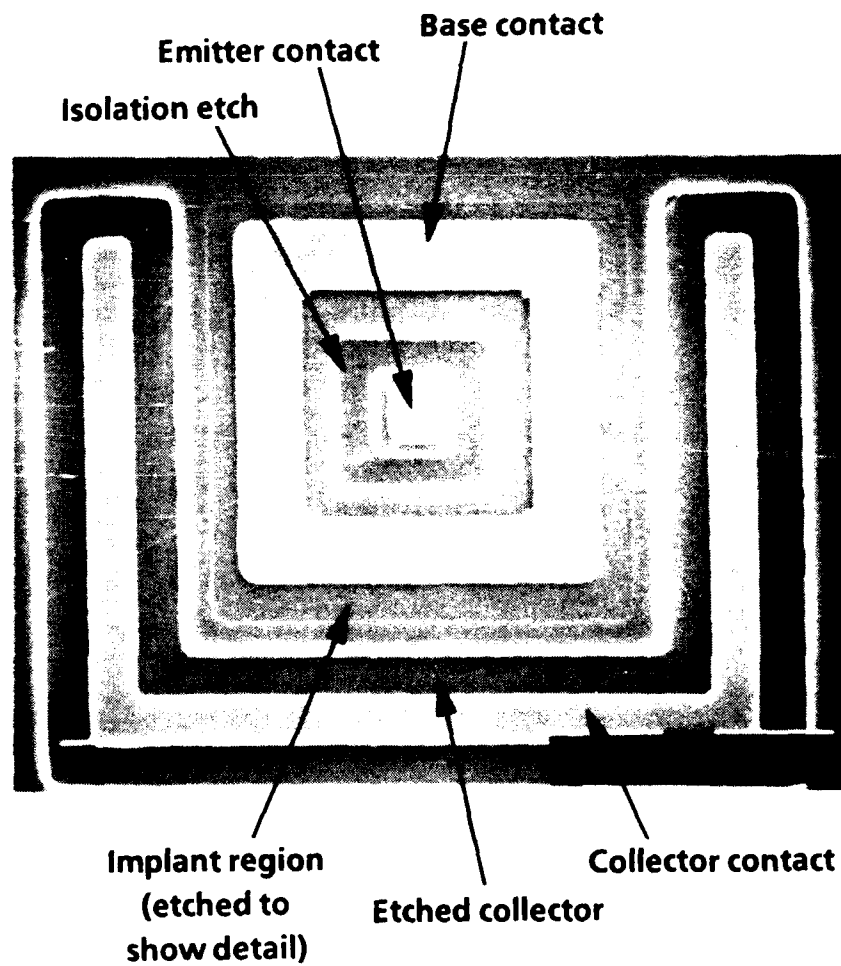


Figure 15. SEM of BiQuaRTT device showing emitter, base, and collector contacts.

Three different base-to-emitter spacings are used in the mask set for different devices. If misalignment causes the etch pattern to expose emitter or base metal, the isolation etch is difficult to control. The largest spacing is 7 μm , where a 3 μm wide etch annulus has a 2 μm space between it and the emitter on one side and another 2 μm between the etch area and the base implant pattern. A 5.5 μm base-emitter spacing uses a 2.5 μm etch width and 1.5 μm spacing. The smallest base-emitter spacing is 4 μm , where a 2 μm etch width has 1 μm spacing. This smallest spacing creates the most challenging alignment of our process, but also creates the lowest base resistances. The widest spacing assures that some of the devices will be processed with no alignment problems.

The isolation etch is a critical step for proper device operation. The etch should proceed through most of the emitter layer but must not penetrate the quantum well region. In fact, it must leave enough n-type material above the well to avoid surface depletion of the well due to Fermi level pinning. The etch process is a tedious one involving etching for short times and checking electrical parameters until the base and emitter contacts are sufficiently decoupled.

There is a test structure designed to aid in this process. It includes two base contacts and an emitter contact that are all large enough to be easily probed. One of the base contacts is surrounded with an isolation trench. One may etch and monitor the emitter-to-base and base-to-base resistance. The goal of the etch is to produce the highest resistance in the emitter-to-base while not degrading the base-to-base resistance. The difficulty is knowing when to stop. This particular test structure, however, is designed to give an early warning. A separate mask level that overlays the isolation etch layer ON THIS STRUCTURE ONLY is used to give the etch trench a slight head start. By pre-etching the structure a few hundred angstroms we may then pattern with the isolation etch mask and etch until base-to-base resistance starts to degrade on this special test structure. Because the isolation etch should not have proceeded that far on the actual devices, this should be an excellent endpoint detection for the isolation etch.

The base-to-emitter isolation depends primarily on surface depletion removing free carriers from a thin remaining layer of emitter material. One method of improving the control of this critical region would be to place a Schottky contact down in the etch trench. By adjusting the voltage on the Schottky contact, the depth of the depletion layer may be adjusted to improve device performance. Two mask layers have been added to the new mask set to explore this possibility.

f. Isolation, Passivation, And Final Metal

After the metal contacts are formed and isolation etch is completed, deep trenches are etched down to the semi-insulating substrate to provide device-to-device isolation. A passivating silicon nitride layer is deposited over all devices. Contact vias are etched down to all devices and a metal bond pad layer is patterned.

g. Two Base Contact Device

Several special devices that include two base contacts are included on the mask set. By applying a very small difference in the voltage on the two base contacts, these devices will allow us to monitor base resistance as a function of tunneling current. This may shed some light on the question of charge build-up in the well during tunneling.

h. Test Structures

The mask set includes several test structures besides the isolation etch structure mentioned above: seven different transmission line structures that measure the sheet resistivity of and contact resistance to different layers, several large transistors for checking devices prior to final metal deposition and bonding, a C-V measurement structure, a set of RTD structures, a Hall bar for measuring quantum well conduction, a final metal step coverage test, and a test structure to measure contact via and nitride passivation quality.

2. Pseudomorphic BiQuaRTT

a. Contact To Well

To make ohmic contact to the quantum well, beryllium is implanted at 50, 80, and 160 keV all at 1×10^{15} ions/cm². This heavy p⁺

implant compensates the n-type doping in the emitter layer and produces a p-type region from the surface down to the p-type quantum well. Experiments with different annealing procedures have shown that a 10 sec anneal at 750°C in a rapid thermal annealing unit does an excellent job of activating the implant. Both Au/Zn and Ti/Pt/Au ohmic metal systems have been used to make contacts to the p-type regions, although we are currently using the latter system because of better adhesion and concerns about Zn diffusion.

Figure 16 is a multiple trace of I-V curves from a test structure on a completed die, showing hole transport through the p-doped well. The different curves show the resistance between two different implanted regions that are separated by varying distances (2, 4, 8, 16, and 32 μm). The I-V responses are reasonably straight and resistances vary almost linearly with spacing. This measurement gives a sheet resistivity of 9.7 $\text{k}\Omega/\text{square}$, which is reasonably close to the 7 $\text{k}\Omega/\text{square}$ expected from the doping level and thickness of the well.

The ohmic behavior of these contacts to the well imply that the tunneling barrier layers are not affecting transport. This is not unexpected, since the very heavy implant doses should produce significant disordering in the double-barrier structure. We have preliminary results from cross-section electron micrographs that indicate significant damage to the double-barrier structure in the implanted regions.

b. The Epitaxial Structure Of The BiQuaRTT

To verify the concept of a hidden ground state in this system, we demonstrate the gradual shifting of the ground-state resonance to lower voltage as In is incorporated into the quantum well of nominally identical structures. Figures 17 and 18 illustrate this effect. It should be noted (Figure 17) that the lowest voltage structure ($y = 0.08$) has a finite zero-bias conductance, since the quantum well state has been lowered below the Fermi level of the GaAs contacts. Upon increasing the In content above this value, the ground state of the quantum well "disappears" (Figure 18) and only resonances from the excited states of the quantum well occur. Structures of this type are suitable for the BiQuaRTT.

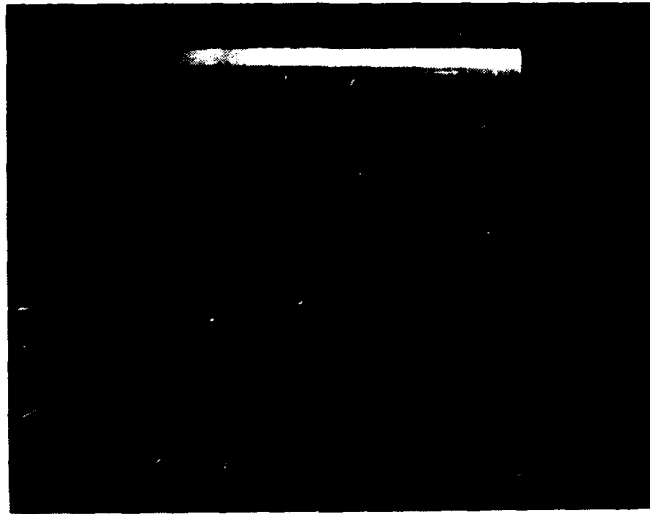


Figure 16. Multiple trace I-V curves of conduction through p-well with implanted contacts at various spacing.

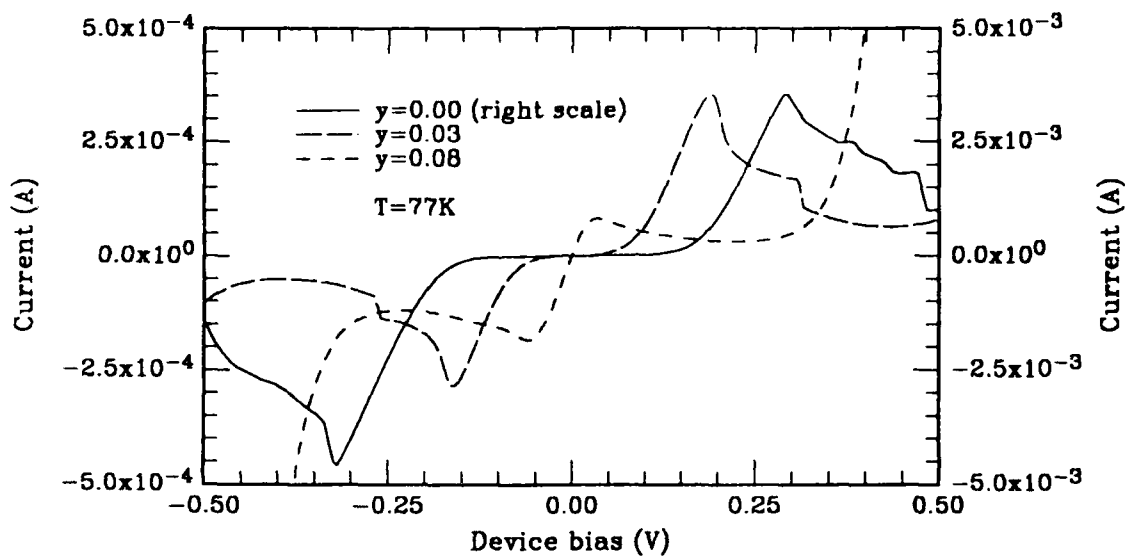


Figure 17. Current-voltage characteristics at 77 K of 50 Å $\text{In}_y\text{Ga}_{1-y}\text{As}$ quantum well/40 Å $\text{Al}_{0.25}\text{Ga}_{0.75}\text{As}$ barrier structures, with $y = 0$, $y \sim 0.03$, and $y \sim 0.08$.

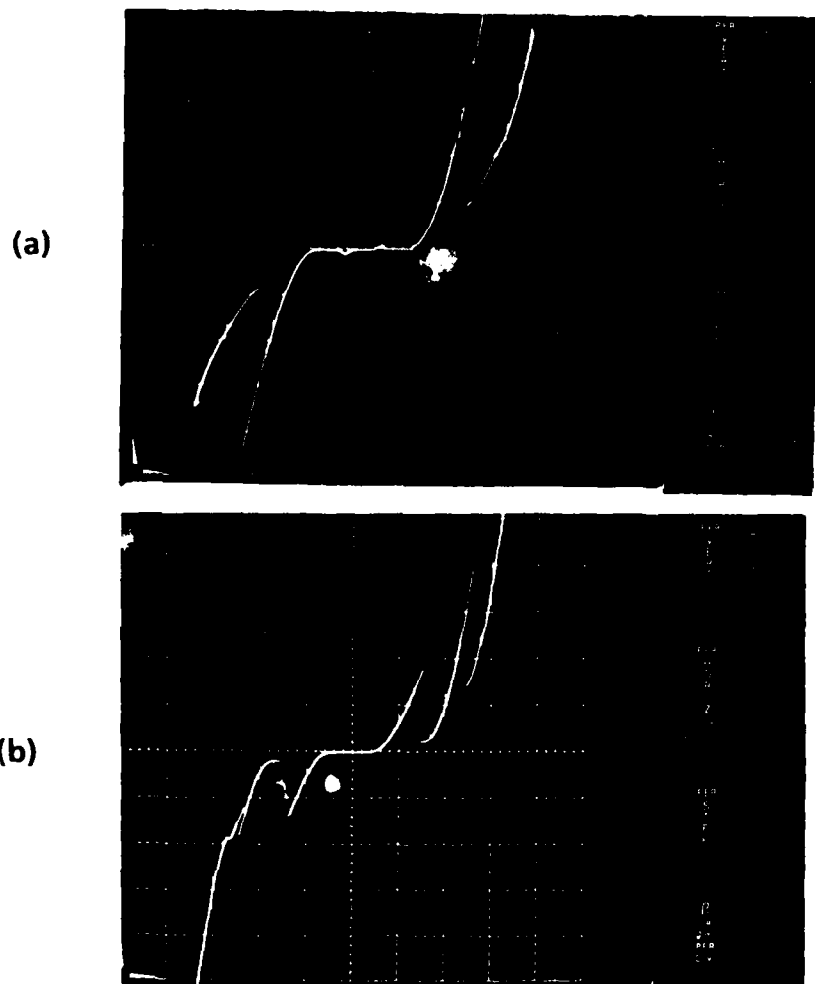


Figure 18. Current-voltage characteristics at 77 K of (a) an 85 Å GaAs quantum well/35 Å AlAs barrier structure (the ground and first excited state resonances are visible), and (b) an identical structure as in (a), with the replacement of the GaAs quantum well with an 85 Å $\text{In}_{0.1}\text{Ga}_{0.9}\text{As}$ quantum well. The ground state is hidden, and the first and second excited state resonances are visible.

The BiQuaRTT structures must also include Be doping in the quantum well. Our calculations indicate that doping levels in the mid-high 10^{18} cm^{-3} range will be required to prevent depletion of the well. We have grown and analyzed a series of resonant tunneling structures with Be doping in the quantum well. Little degradation in the peak-to-valley ratio is seen until doping levels reach the low 10^{18} range, and resonance is destroyed for higher doping levels. This is presumably due to excess scattering by the Be dopants.

This negative result seemed to imply that the realization of tunneling structures with high doping levels in the quantum well would be difficult at best. However, we noticed in the fabrication of resonant tunneling structures that the incorporation of ambient impurities (via growth interruptions) at the tunnel barrier interfaces dramatically impacts scattering, whereas incorporation of impurities in the center of the quantum well has little effect. Thus, we suspected excess diffusion of Be through the structure (especially at the crucial tunneling interfaces) to be responsible. SIMS profiles of these structures verified an anomalously large Be concentration throughout the entire resonant tunneling structure.

To attack this problem, we decided to delta-dope the quantum well and modify the substrate temperature profile to localize the impurities to the quantum well. A test structure with an AlAs barrier, a delta-doped quantum well, and a GaAs cap layer was grown for SIMS investigation of Be diffusion for delta-doping. The results by SIMS profiling show, to within the resolution possible by SIMS, that the localization by delta-doping appears to have worked.

Thus, BiQuaRTT structures were grown utilizing this technique. The I-V characteristics of a control structure and one with delta-Be doping (to mid 10^{18} cm^{-3}) were measured and compared. The doped structure showed little degradation.

After implant, all of these structures were annealed (RTA) to 850°C , and the tunneling characteristics before and after anneal compared. This anneal is a concern since the Be-dopant may diffuse throughout the

structure at this temperature. None of the structures exhibited degradation in their I-V characteristics, implying that the RTA anneal is sufficiently short to prevent any Be diffusion through the structure.

Lateral conductivity measurements (of the p-doped well) were performed after p-ohmics were formed to the implanted region. For the conventionally doped samples, the results were as expected: conduction through the quantum well was observed for wells p-doped sufficiently high, whereas for less doping (such that the quantum well is depleted), no lateral transport was observed. This was not the case for the delta-doped samples; all samples exhibited depleted wells, even those that should have had sufficient p-dopant to keep the well undepleted. This density was determined by bulk growth parameters, assuming no reevaporation of Be.

With the development of better modeling tools, we then simulated these structures to determine exactly the hole density in the well. We then commenced concurrent fabrication and measurement of samples for SdH measurements of the hole density of the well. It was quickly realized that (1) the screening of the n^+ regions in the GaAs contacts tends to deplete the well more drastically than initially realized; and (2) if the well is not depleted, we should observe NO resonance in a two-terminal configuration. This was a crucial point in our understanding of these structures.

Modeling of the structures showed that for the structures tested to date, the free hole density in the quantum well is less than $1 \times 10^{14}/\text{cm}^3$, despite the fact that the quantum well doping exceeds 1×10^{18} . The hole density is decreased because the internal field of the structure moves a large fraction of the free hole charge out of the quantum well.

There are two ways that we can increase the free hole density in the quantum well: one is to further increase the quantum well doping, the other is to reduce the internal field of the heterostructure. We believe that we are at or near the practical limit of dopant level in the well. The internal field however can be reduced significantly by reducing the n-type doping in the structure near the well. In particular, the collector may be lightly doped, since it is not required to supply electrons.

Another problem we have consistently seen in our devices is a significant leakage apparently from base to collector. In an attempt to keep charge carriers that are not a part of the resonant tunneling current better confined in the well, we are trying to produce deeper wells (more In content) and in some cases increasing the bandgap of the collector by adding Al (raised collector).

c. Redesigned Epitaxial Structure

We thus redesigned the BiQuaRTT epitaxial structures. Several versions are presently being worked on. Four of these are highlighted below.

(1) Structure A--Deep Well BiQuaRTT, Lightly Doped Collector

To ensure that the ground states are well hidden, the InGaAs well is very deep. Additionally, the contact buffer is increased (250 Å) and, most importantly, the collector is very lightly doped. This lessens the space charge effect by two on the quantum well, and the only side that need be heavily doped is the emitter. The structure is as follows:

Semi-insulating substrate

GaAs undoped buffer

1.0 μm n⁺ GaAs (2×10^{18}) collector contact

0.5 μm n GaAs (5×10^{16}) collector

250 Å undoped GaAs (buffer)

30 Å undoped AlAs (RTD barrier)

100 Å Be-doped (1×10^{19} , center 40Å) InGaAs, $y = 0.22$ (RTD QW)

30 Å undoped AlAs (RTD barrier)

250 Å undoped GaAs (buffer)

0.5 μm n⁺ GaAs (2×10^{18}) emitter.

The prediction is greater than $1 \times 10^{18}/\text{cm}^3$ holes in the well.

(2) Structure B--Wide Well BiQuaRTT, Lightly Doped Collector

A variation on Structure A, but using a wider well. This structure was done to compare the indirect AlAs barriers with direct AlGaAs barriers.

Semi-insulating substrate

GaAs undoped buffer

1.0 μm n^+ GaAs (2×10^{18}) collector contact

0.5 μm n GaAs (5×10^{16}) collector

250 Å undoped GaAs (buffer)

50 Å undoped AlGaAs, $x = 0.40$ (RTD barrier)

150 Å Be-doped (1×10^{19} , center 50 Å) InGaAs, $y = 0.08$ (RTD QW)

50 Å undoped AlGaAs, $x = 0.40$ (RTD barrier)

250 Å undoped GaAs (buffer)

0.5 μm n^+ GaAs (2×10^{18}) emitter.

(3) Structure C--Wide Well BiQuaRTT, Raised & Lightly Doped Collector

The difference here from Structure B is that the collector now has a wider bandgap to better hide the ground states.

Semi-insulating substrate

GaAs undoped buffer

1.0 μm n^+ GaAs (2×10^{18}) collector contact

0.25 μm n^+ AlGaAs, $x = 0.20$ (2×10^{18}) collector contact

0.5 μm n AlGaAs, $x = 0.20$ (5×10^{16}) collector

250 Å undoped AlGaAs, $x = 0.20$ (buffer)

50 Å undoped AlGaAs, $x = 0.40$ (RTD barrier)

150 Å Be-doped (1×10^{19} , center 50 Å) InGaAs, $y = 0.08$ (RTD QW)

50 Å undoped AlGaAs, $x = 0.40$ (RTD barrier)

250 Å undoped GaAs (buffer)

0.5 μm n^+ GaAs (2×10^{18}) emitter.

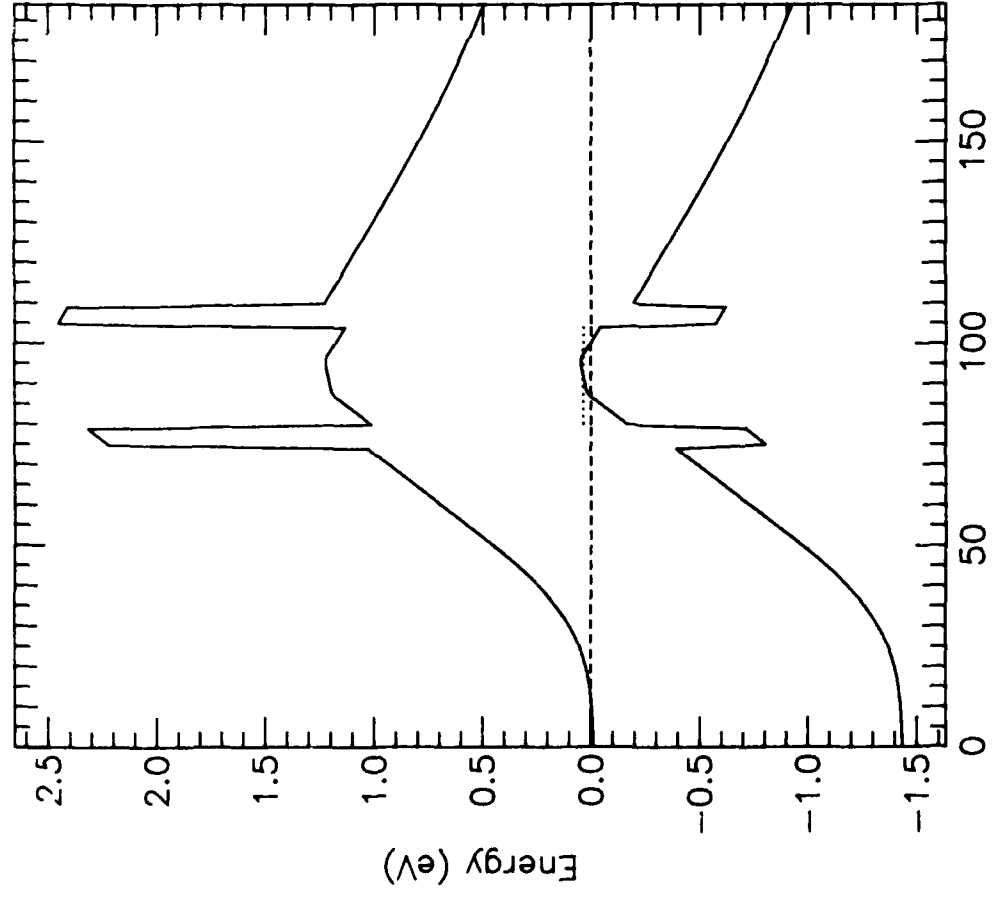
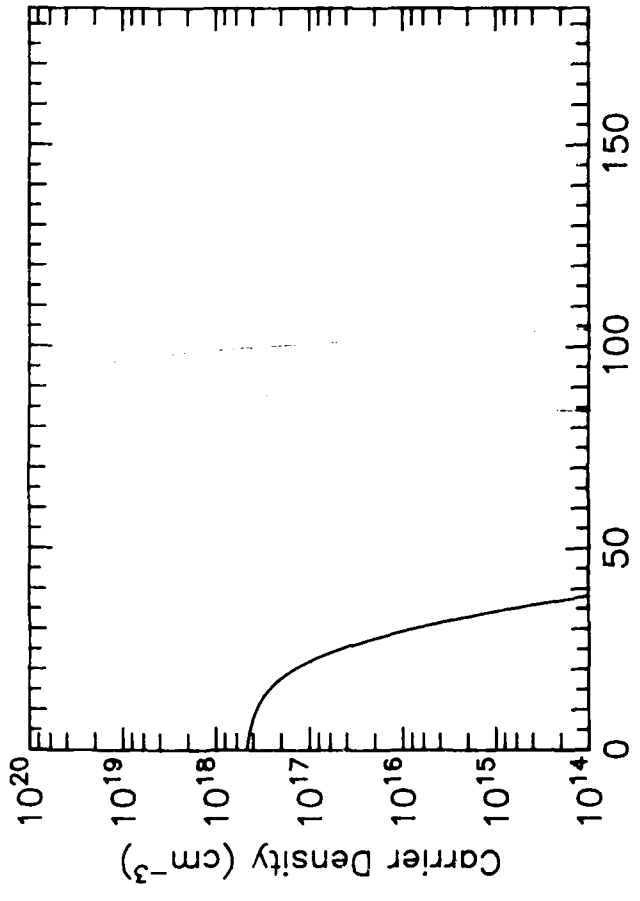
(4) Variation of Structure B

A fourth structure, a variation on Structure B, has recently yielded our first room-temperature current gain in the AlAs/InGaAs/AlAs materials system. The layer structure is outlined below with its energy band diagram and charge distribution (under zero bias) shown in Figure 19.

n^+ substrate

0.5 μm n^+ GaAs (2×10^{18}) collector contact

R2324



$V_e=0.00$ $V_b=0.00$ $V_c=0.00$

T = 300 K
SIMULATION DID NOT CONVERGE
24 AUG 1988 16:43

Thickness	Composition	Doping
50 nm	GaAs	N $5.0 \times 10^{17} \text{ cm}^{-3}$
25 nm	GaAs	N $1.0 \times 10^{14} \text{ cm}^{-3}$
5 nm	AlAs	N $1.0 \times 10^{14} \text{ cm}^{-3}$
7 nm	$\text{In}_{0.23}\text{Ga}_{0.77}\text{As}$	N $1.0 \times 10^{14} \text{ cm}^{-3}$
11 nm	$\text{In}_{0.23}\text{Ga}_{0.77}\text{As}$	P $1.0 \times 10^{19} \text{ cm}^{-3}$
7 nm	$\text{In}_{0.23}\text{Ga}_{0.77}\text{As}$	N $1.0 \times 10^{14} \text{ cm}^{-3}$
5 nm	AlAs	N $1.0 \times 10^{14} \text{ cm}^{-3}$
25 nm	GaAs	N $1.0 \times 10^{14} \text{ cm}^{-3}$
50 nm	GaAs	N $5.0 \times 10^{16} \text{ cm}^{-3}$

Figure 19. Equilibrium potential and charge density profiles for the pseudomorphic BiQuaRTT.

0.5 μm n GaAs (2×10^{16}) collector
 250 Å undoped GaAs (buffer)
 50 Å undoped AlAs (RTD barrier)
 250 Å InGaAs (1×10^{19} , center 100 Å) $y = 0.2$ (RTD QW)
 50 Å undoped AlAs (RTD barrier)
 250 Å undoped GaAs (buffer)
 0.2 μm n GaAs (5×10^{17}) emitter
 0.3 μm n⁺ GaAs (2×10^{18}) emitter contact

The primary variation between this structure and Structure B is that the quantum well is deeper ($y = 0.2$) and wider (250 Å). For the 250 Å base, assuming X point AlAs barriers, approximately ten excited states can be expected with average energy spacing of about 100 meV. These levels are not shown in Figure 19, since they are not bound (hence the simulation convergence warning). Results for this structure are described below in Section II.B.2.d.

Structures A, B, and C were preceded with a series of "control" samples, without Be-doping, to evaluate the band structure and ensure that the quantum well states were hidden as expected. For example, Structure A without In in the well exhibited a $n = 1$ resonance at $V_{ce} = 50$ mV, an $n = 2$ resonance at 320 mV, and an $n = 3$ resonance at 700 mV. With In, the structure was designed (coincidentally) to have the $n = 2$ state at approximately the same position as where the $n = 1$ was. With In, the structure exhibited a resonance ($n = 2$) at 60 mV, ($n = 3$) at 300 mV, and ($n = 4$) at 800 mV, increased as expected over the no-In case due to the deeper well.

When the structures were then Be-doped, we observed a phenomenon previously not seen in BiQuaRTT structures--no conduction (prior to breakdown, assumed to be avalanche breakdown) from emitter to collector. In hindsight, this is exactly what should be observed if the quantum well has free holes. This implies that the epitaxial structure is, probably for the first time, correct. After implantation, contact to and conductivity through the base was easily observed.

d. BiQuaRTT Device Results

Room-temperature gain has been obtained in the pseudomorphic BiQuaRTT structure shown in Figure 19. Processing of devices A, B, and C are nearly completed, with observed current gain at 77 K.

In Figure 20, the room-temperature common-emitter transistor characteristics for the BiQuaRTT are shown. A gain of greater than five is seen in this device and as high as nine has been measured. The devices show a large collector offset voltage that is currently being investigated. Apparent resonance phenomena are observed near collector-emitter breakdown and at high base current injection. Analysis of these characteristics is presently under way and will be reported in the next quarter.

Characteristics of Structures A, B, and C large area devices that could be probed at this stage are very promising. The structures exhibit negative transconductance (voltage biasing) and greater than unity current gain (current biasing). At 77 K, the structure exhibits a current gain as great as 1.2. The large area device is expected to have a large leakage current, and results from small area devices will be forthcoming.

In parallel with this effort, we have been working under a similar contract funded by AFWAL for the development of this structure in the pure AlGaAs embodiment. The vehicle chosen here used either AlGaAs injectors of superlattice injectors. Similar changes to this structure exhibited the same results (using superlattice injectors). This structure exhibited a current gain as high as 450. Details of this result are shown in Appendix A.

3. QuESTT

a. Baseline Structure

(1) Progress

During this report period, steady progress has been made toward the achievement of the QuESTT. As this structure was originally envisioned, the tunneling current modulation is achieved by forming a regrown contact to the quantum well of a resonant tunneling diode. Much of the process technology necessary for realization of this structure is now in place. Our accomplishments include: (1) demonstration of a reactive ion etch

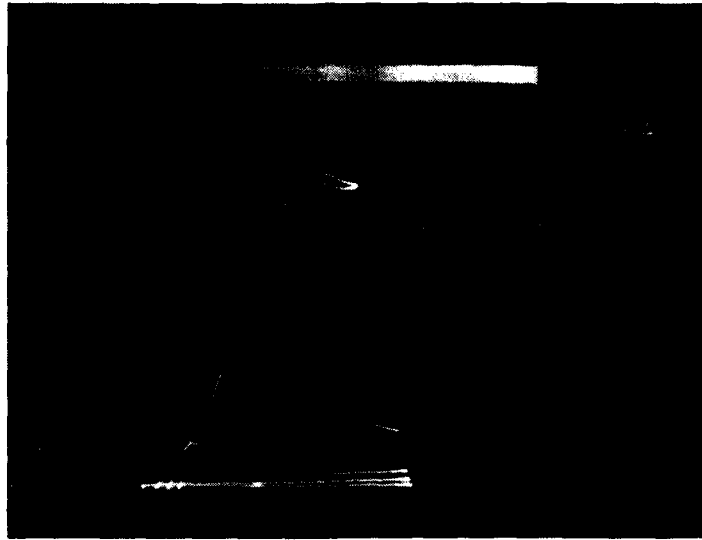


Figure 20. Room-temperature common-emitter transistor characteristics for the pseudomorphic BiQuaRTT.

process [Appendix B] that stops on AlGaAs and InGaAs layers, (2) development of a post-etch cleaning process suitable for MBE regrowth, (3) successful single-crystal regrowth of InGaAs layers, and (4) full fabrication of regrown QuESTT devices. QuESTTs demonstrating current gain have not been completed, but tests on the completed devices do not reveal any intrinsic problems with the concept.

Key to the fabrication of the QuESTT transistor is the selective regrowth of a low-bandgap semiconductor on the quantum well of a resonant tunneling diode. A first step in this fabrication is the selective removal of the GaAs overlying the quantum well. Experiments with the $\text{CCl}_2\text{F}_2:\text{He}$ reactive ion etch have shown that GaAs etching can be stopped on a 35 Å AlAs/85 Å InGaAs/35 Å AlAs resonant tunneling structure. This etch is known to be highly selective for GaAs with low AlGaAs etch rate, but had not been shown to be effective on the thin layers comprising this device.

To determine whether the InGaAs plays a role in the etch stop, a structure consisting of a single 50 Å InGaAs layer ($x < 0.15$) sandwiched between thick GaAs regions was etched. The etch stopped with mirror finish on the 50 Å layer. This capability may have other uses in the QuESTT and BiQuaRTT fabrication process since precise control of the etch depth can be made without the introduction of an electronic barrier.

To determine whether the surface remaining after the RIE etch is suitable for MBE regrowth, x-ray photoelectron spectroscopy (XPS) was used to examine the near-surface region. The wafer, a GaAs layer above a thick AlGaAs layer, was patterned with AZ photoresist to simulate the patterning necessary for the QuESTT. After RIE etching, the wafer was subjected to an acetone spray to remove the photoresist, a rinse in DI water, and a nitrogen blow-dry. Within five minutes of this treatment, the wafer was under vacuum in the analysis chamber. The XPS measurements reveal a relatively clean GaAs surface. Immediately upon introduction into the chamber we found a surface with 10.5% C and 17.9% O, as well as a mixture of Ga and As oxides. The samples were removed in late afternoon and allowed to sit exposed to air overnight. The next morning the sample was loaded and measured again. We

found that the C had been desorbed in the night and we saw the presence of AlGaAs and Al₂O₃. No evidence of fluorines or chlorines was found.

Transmission electron microscopy (Figure 21) has revealed the successful regrowth of InGaAs on the quantum well of the QuESTT. The selective etching is performed with a CCl₂F₂ and He reactive ion etch, which is found to effectively stop on buried layers of AlGaAs and InGaAs. In Figure 21 the etch appears to consume or chemically alter the first 35 Å AlAs layer leaving an atomically smooth interface for regrowth of the thick InGaAs contact layer. The InGaAs well layer is 85 Å.

Dislocations in the regrown InGaAs are apparent. These arise because the thickness of the regrown contact layer, 2000 Å, exceeds the critical layer thickness for dislocation formation. In addition, we have observed microcontaminants that were left on the wafer surface after selective etching and clean-up. These amorphous particles are the source of the larger defects apparent in the regrown InGaAs. While the elemental constitution of these particles has not been identified, it has been found that they are effectively removed by a hydrofluoric acid-based etchant after the selective etch and before loading for MBE regrowth.

Another feature of the etching is the undercut, which produces a shadowing effect during the MBE growth and disconnects the regrowth of InGaAs between emitter and base. Device measurements show poor electrical contact to the base. We suspect that this may result from depletion of the quantum well electrons from the free-RIE etched surface that was not regrown. This problem may be solved by utilizing an alternative device orientation, since the reactive ion etch is known to have an etch profile dependent on crystallographic orientation (Appendix B). A circular device geometry has been incorporated in a recently completed mask set that effectively tests all base regrowth orientations in a single fabrication sequence.

An initial set of three AlAs/InGaAs/AlAs QuESTT structures differing in quantum well doping density were regrown and fabricated. The dopings were chosen to be $1 \times 10^{17}/\text{cm}^3$, 1×10^{16} , and undoped to minimize degradation of the resonant tunneling characteristics by ionized impurities.

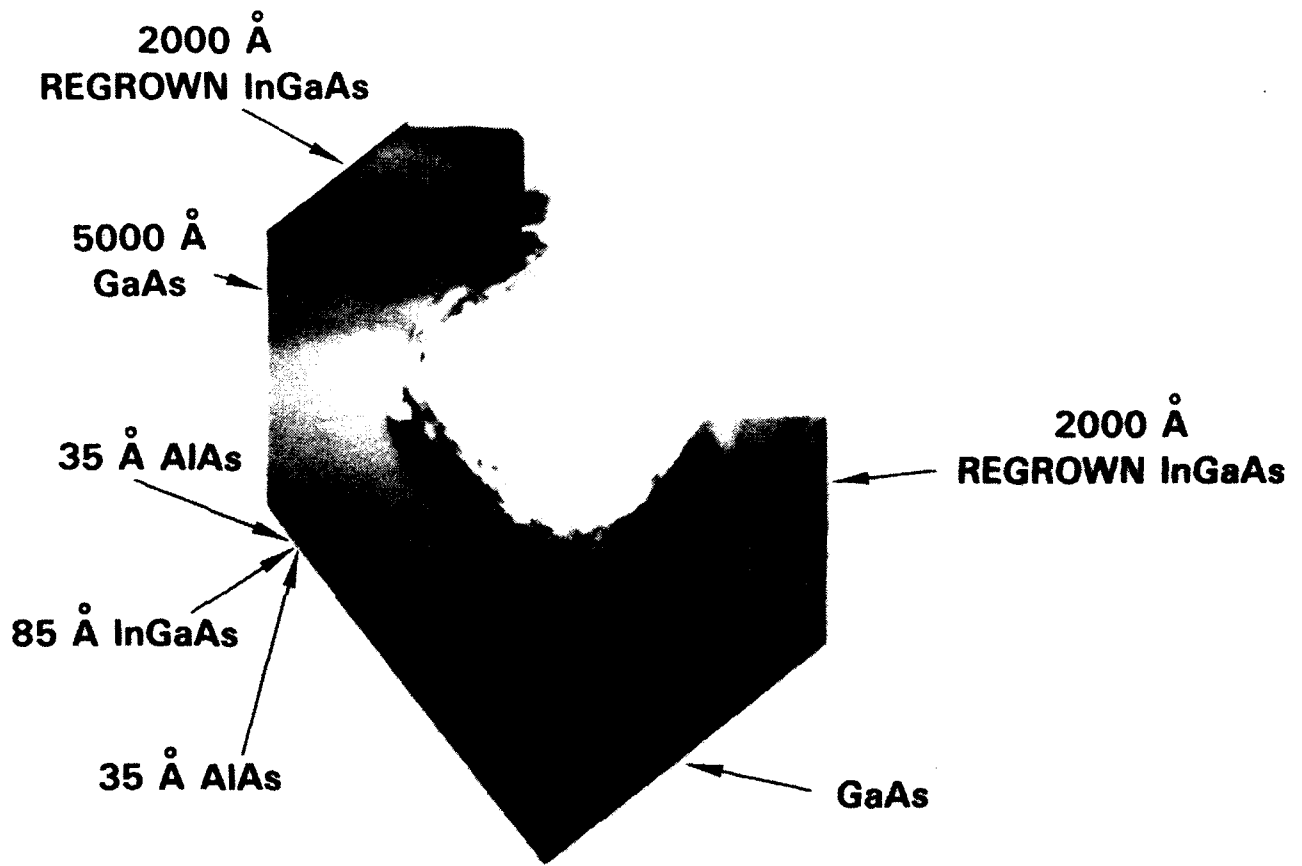


Figure 21. Cross section TEM of selectively etched (RIE) and regrown QuESTT structure.

Following regrowth and three-terminal device fabrication, both the undoped and $1 \times 10^{16}/\text{cm}^3$ samples show NDR; however, the $1 \times 10^{17}/\text{cm}^3$ doped sample did not. Devices fabricated on these structures showed neither good electrical contact to the base nor three-terminal gain.

Our modeling of these structures, using the QuESTT model calculation developed after growth of these structures, shows that there is insufficient electron density in the base to provide for ohmic base contact. These simulations show that the electron density can be increased to greater than $1 \times 10^{18}/\text{cm}^3$ without doping the well or barriers by using In mole fractions of 20% or more. The high electron density is achieved by creating a deep quantum well bound state that is fully occupied. Simulations also show that the potential barrier seen by electrons approaching the quantum well from the contact will be greater if the material is not degenerate, so lower contact doping can improve the tunneling characteristics.

Two QuESTT structures that incorporate these features have been grown and device fabrication begun. Examination of the Au/Ge/Ni ohmic base contact revealed that the anneal sequence resulted in electrical connection of collector and base in these structures. Both rapid thermal anneal and nonalloyed regrown contact processes are now being pursued.

b. Variations

(1) MBE Thermal Etch And Regrowth

A novel etching/regrowth technique that involves sublimation of GaAs at 750°C and subsequent regrowth of epitaxial material has been developed. We have continued to explore the technique. At 750°C , while maintaining an As flux similar to that used for GaAs growth, the GaAs/AlGaAs etch ratio is at least 100:1. We have demonstrated that we may stop on a layer of 40% AlGaAs as thin as 50 Å.

Figure 22 is a TEM cross section of an etched and regrown sample. The original epitaxial structure consisted of a 1000 Å AlGaAs cap layer, 5000 Å GaAs, a 50 Å AlGaAs layer, a 50 Å GaAs quantum well, and 2000 Å of AlGaAs on a GaAs substrate. A portion of the AlGaAs cap layer was patterned and chemically etched prior to reinserting in the MBE chamber. In

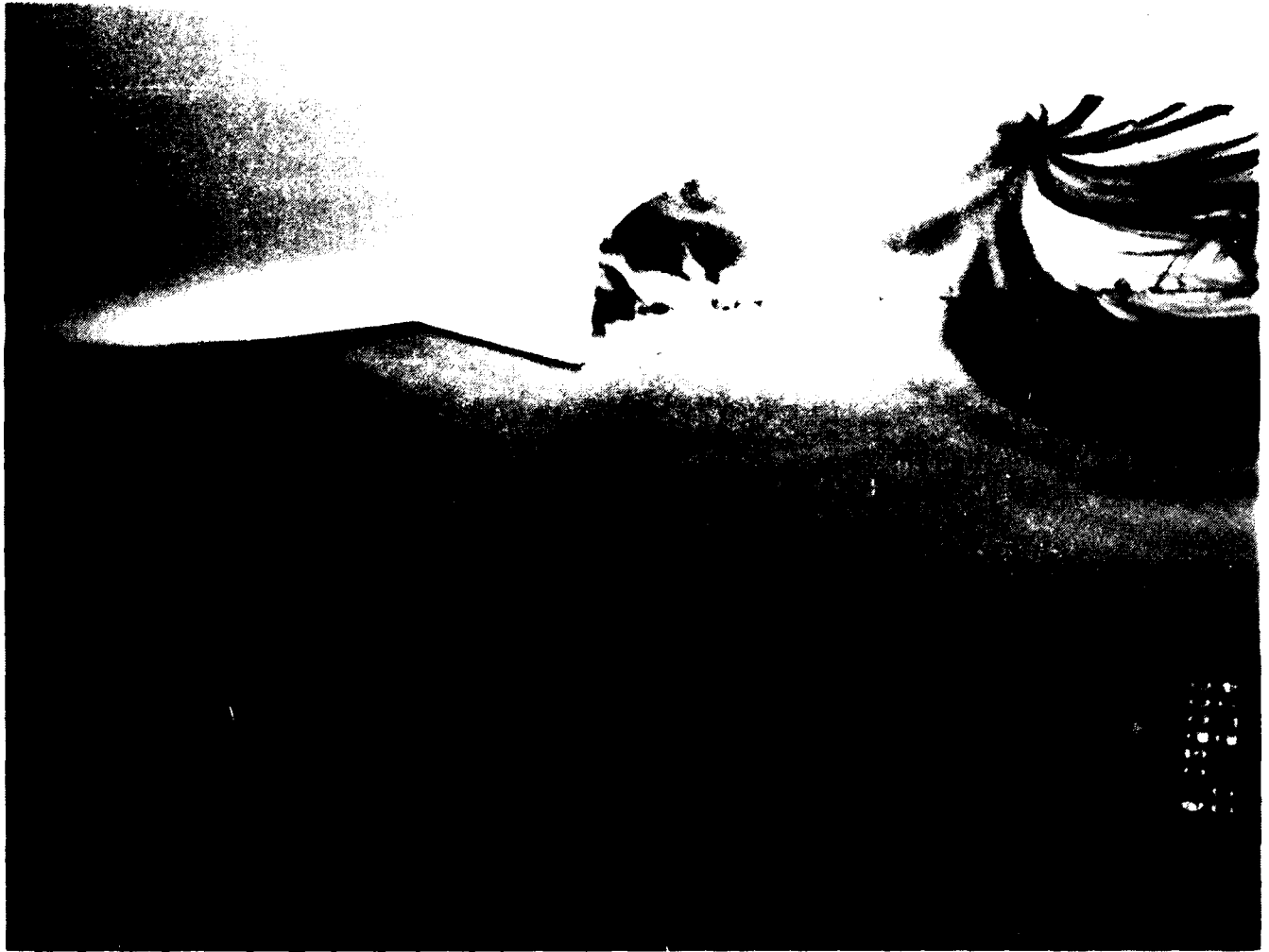


Figure 22. Cross section TEM of selectively etched (thermal MBE) and regrown QuESTI structure.

the MBE chamber, 5000 Å of GaAs was etched down to the 50 Å AlGaAs etch stop. Subsequently, 5000 Å of GaAs was regrown.

Figure 22 shows that the material regrown in the etched portion of the sample (on the left) appears to be quite good with few defects despite the existence of a large number of inclusions at or near the regrowth interface. Furthermore, the sidewall coverage is excellent.

On the other hand, higher magnification micrographs showed some penetration of the 50 Å AlGaAs layer, and a general roughness to the heterostructure interfaces, which could be due to diffusion resulting from the extended time at 750°C. This diffusion is a serious problem that could destroy the resonant tunneling behavior. We have just completed an experiment that subjected RTDs to a wide range of thermal cycles. The preliminary data suggest that an extended time at 750°C should not seriously degrade tunneling performance. This result will allow further attempts to use the thermal etch and regrowth technique to fabricate QuESTT devices.

(2) Isolation Etch Stop

For both QuESTT and BiQuaRTT devices, base-emitter isolation is an important issue. In the regrown QuESTT structure the isolation is provided by a heterojunction barrier; however, in the BiQuaRTT and alternate QuESTT structures, an isolation etch step must be performed. One possible approach to improving the reproducibility of the isolation etch step would be to introduce an etch-stop layer at the appropriate position. The difficulty with this plan is that until recently, only high-bandgap material (AlGaAs) provided a reliable etch stop. Including an additional AlGaAs layer would introduce an unacceptable barrier.

Recently, however, the ability to stop on thin layers of InGaAs with reactive ion etching has been demonstrated both by workers at Varian and here at TI. In fact, we have developed two different InGaAs etch stop processes. The CCl_2F_2 etch (mentioned above) used in conjunction with QuESTT regrowth and a BCl_3 etch process both stop on 10% InGaAs as thin as 100 Å. The advantage of the BCl_3 etch is that it will etch through AlGaAs layers while the CCl_2F_2 process will stop on either AlGaAs or InGaAs.

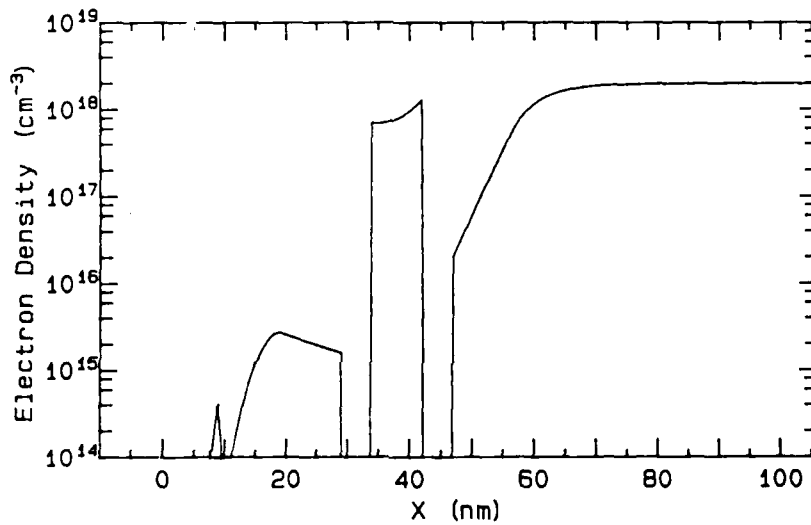
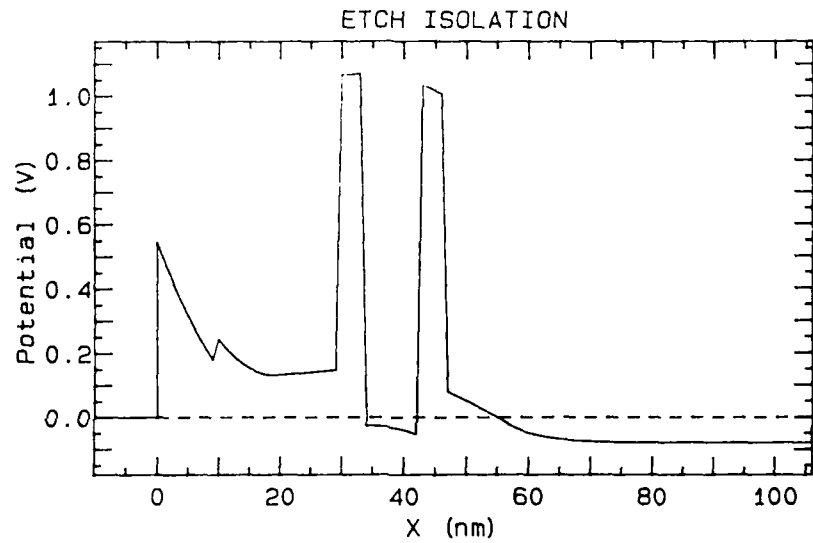
A thin InGaAs layer grown after the double-barrier structure will place a quantum well in the structure, but this should not have a strong effect on tunneling transport through the device. By using one of these RIE etch stop techniques, the etch will reliably stop at the same depth in the structure. The position of this layer in the epitaxial structure should be such that surface depletion should produce only a small number of free carriers in the layer above the well, but should not reduce the carrier concentration in the well.

Figure 23 shows a simulation of the band structure and carrier density of a QuESTT-type device where a 100 Å of 10% InGaAs has been inserted and used as an etch stop. The exact epitaxial structure is the following:

<u>Thickness</u>	<u>Composition</u>	<u>Doping Level</u>
100 Å	10% InGaAs	2×10^{18}
100 Å	GaAs	2×10^{18}
100 Å	GaAs	1×10^{14} (undoped)
40 Å	AlAs	1×10^{14} "
90 Å	20% InGaAs	1×10^{14} "
40 Å	AlAs	1×10^{14} "
100 Å	GaAs	1×10^{14} "
500 Å	GaAs	2×10^{18}

The results of the simulation demonstrate that the number of free carriers in the InGaAs and GaAs layers above the double-barrier structure is two orders of magnitude less than in the well. At 77 K, the model predicts that all free carriers above the well are depleted, while the carriers in the quantum well are unaffected.

We should soon grow RTD structures that include this InGaAs etch stop layer to test the effect of that layer on tunneling current. One additional concern is that damage from the RIE process might deplete the quantum well. Only experimentation will answer that question, but the very low ion energy used in the BCl_3 etch process should minimize the risk.



Temperature = 300 K
Schottky barrier = 0.6 eV

7 SEP 1988
13:22

Figure 23. Simulation of the band structure and carrier density of a QuESTT type device that includes an InGaAs layer used as an etch stop. The exact epitaxial structure is:

Thickness	Composition	Doping Level
----- SURFACE -----		
100 Å	10% InGaAs	2×10^{18}
100 Å	GaAs	2×10^{18}
100 Å	GaAs	1×10^{14} (undoped)
40 Å	AlAs	1×10^{14} "
90 Å	20% InGaAs	1×10^{14} "
40 Å	AlAs	1×10^{14} "
100 Å	GaAs	1×10^{14} "
500 Å	GaAs	2×10^{18}

(3) Plans

There does not appear to be any technical impediment to realization of the QuESTT. Processing problems have been identified and are presently being corrected. In addition, structures that incorporate a thin 20 Å to 50 Å InAs notch in the center of the quantum well have been grown for selective etch and regrowth. The use of the InAs notch pulls the ground state in the quantum well still further, which is expected to improve connection to the base.

Further experiments on the MBE thermal etch and regrowth will be undertaken. RTD structures with a thin InGaAs layer above and near the double-barrier structure will be grown to test what effects the InGaAs layer has on tunneling transport and to explore better base-to-emitter isolation.

III. CONCLUSIONS/RECOMMENDATIONS

Based on the results obtained during the first year of effort, it is concluded that both the pseudomorphic BiQuaRTT and the QuESTT are viable devices. This conclusion is further supported for the pseudomorphic BiQuaRTT by results obtained on a lattice-matched version of the BiQuaRTT under a separate Air Force contract. Although a working QuESTT has not yet been realized, modeling of the device indicates that it will operate, and the process development activity has solved all of the known fabrication problems. Devices incorporating these features are being fabricated.

It is recommended that the program be continued along the lines outlined in the proposal, including optimization of both devices, with emphasis gradually shifting from the BiQuaRTT to the QuESTT, because of the latter device's greater potential for downscaling. A decision on whether or not to pursue the optically switched resonant tunneling device discussed in the proposal should also be made during the coming year. The subcontract with Stanford University, inception of which has been delayed by protracted contract negotiations, should begin to enhance the device characterization activity.

REFERENCES

1. R. T. Bate in VLSI Handbook, ed. by N. G. Einspruch (Academic Press, New York, 1985), Ch. 35, p. 615.
2. L. L. Chang, L. Esaki, and R. Tsu, Appl. Phys. Lett. 24, 593 (1974).
3. T. C. L. G. Sollner, et al., Appl. Phys. Lett. 43, 588 (1983).
4. T. J. Shewchuk, P. C. Chapin, P. D. Coleman, W. Kopp, R. Fisher, and H. Morkoc, Appl. Phys. Lett. 46, 508 (1985).
5. M. A. Reed, Superlattices and Microstructures 2, 65 (1986).
6. R. W. Keyes, Science 230, 138 (1985).
7. F. Capasso and R. A. Kieh1, J. Appl. Phys. 58, 1366 (1985).
8. N. Yokoyama et al., Jap. J. Appl. Phys. 24, L853 (1985).
9. A. R. Bonnefoi, T. C. McGill, and R. D. Burnham, IEEE Electron Device Lett. EDL-6, 636 (1985).
10. T. C. L. G. Sollner et al., Proceedings IEEE/Cornell Conference on Advanced Concepts in High Speed Devices and Circuits, 252 (1985).
11. A. F. J. Levi, J. R. Hayes, P. M. Platzman, and W. Wiegmann, Phys. Rev. Lett. 55, 2071 (1985).
12. M. Heiblum, M. I. Nathan, D. C. Thomas, and C. M. Knodler, Phys. Rev. Lett. 55, 2200 (1985).
13. H. Morkoc, unpublished presentation at Workshop on Compound Semiconductor Microwave Materials and Devices, San Francisco, CA. (February 1986).
14. M. A. Reed and J. W. Lee, Appl. Phys. Lett. 50, 845 (1987).
15. N. Kluksdahl et al., unpublished.
16. R. K. Mains and G. I. Haddad, "Numerical Considerations in the Wigner Function Modeling of Resonant-Tunneling Diodes," submitted to J. Computational Phys.
17. D. D. Coon and H. C. Liu, Appl. Phys. Lett. 47, 172 (1985).
18. A. M. Kriman, N. C. Kluksdahl and D. K. Ferry, Phys. Rev. B 36, 5953 (1987).

APPENDIX A

REALIZATION OF A THREE-TERMINAL RESONANT TUNNELING DEVICE:
THE BIPOLAR QUANTUM RESONANT TUNNELING TRANSISTOR (BiQuaRTT)

3
SATN

Realization of a Three-Terminal Resonant Tunneling Device: The Bipolar Quantum Resonant Tunneling Transistor (BiQuaRTT)

M. A. Reed, W. R. Frensley, R. J. Matyi,
J. N. Randall, A. C. Seabaugh, and H.-L. Tsai

Texas Instruments, Incorporated
Dallas, TX 75265

ABSTRACT

A new three-terminal resonant tunneling structure in which current transport is controlled by directly modulating the potential of the quantum well is proposed and demonstrated. Typical current gains of 50 at room temperature are observed.

Resonant tunneling^{1,2} provides a controllable current transport mechanism in semiconductor heterostructures. Recent attention has been focused upon exploiting this transport mechanism in three-terminal device configurations.³⁻⁶ Many of these proposed and fabricated devices show behavior which could equally well be obtained from the series connection of a conventional semiconductor device and a resonant-tunneling diode.⁷ This paper presents a new *Bipolar Quantum Resonant Tunneling Transistor* (BiQuaRTT) in which the tunneling current is directly controlled by modulating the potential *inside* a quantum well.⁸

The BiQuaRTT consists of a resonant-tunneling diode structure in which the quantum well is doped p-type and separately contacted. It operates in a manner similar to a conventional bipolar transistor in that the potential in the base (i.e., the quantum well) is controlled by the density of holes as established by the Fermi level of the base contact. Operation via electron tunneling, however, imposes new constraints on the structure of the device. Because the resonant quantum state necessarily lies above the local conduction band, the conduction band in the emitter must be biased to an energy higher than that in the base, to obtain sufficient tunneling current. If a bipolar device were to be built in a conventional resonant-tunneling diode structure where the bandgaps of the quantum well and the two contacting layers are equal, such a bias condition would produce catastrophic leakage currents in the parasitic pn junctions at the base contact. These leakage currents are suppressed by employing wider-bandgap material in the emitter and collector layers of the BiQuaRTT.

A number of options exist for the creation of wider-bandgap regions in the emitter and collector (with respect to the quantum well). One option is to utilize a $\text{Al}_x\text{Ga}_{1-x}\text{As}$ emitter / $\text{Al}_y\text{Ga}_{1-y}\text{As}$ tunnel barrier / $\text{Al}_z\text{Ga}_{1-z}\text{As}$ quantum well structure ($y > x > z > = 0$). Another is to utilize multi-material systems, such as a

GaAs emitter / $\text{Al}_x\text{Ga}_{1-x}\text{As}$ tunnel barrier / $\text{In}_y\text{Ga}_{1-y}\text{As}$ quantum well structure.⁹ A third option, implemented here, is to create a wider-bandgap material in the emitter/collector by using superlattices; i.e., a $(\text{GaAs}/\text{Al}_x\text{Ga}_{1-x}\text{As})$ superlattice emitter / $\text{Al}_y\text{Ga}_{1-y}\text{As}$ tunnel barrier / GaAs quantum well structure. The bottom of the first conduction band miniband serves to emulate a homogeneous alloy raised injector region. In the present structure, a single Al source was used ($x=y$), though clearly more complex engineering can be obtained with multiple sources.

Figure 1 shows a schematic band diagram of the epitaxial structure. The structure was grown on a semi-insulating (Cr-doped) GaAs substrate using a Riber 2300 MBE system. The structure consisted of a 1.0 micron undoped GaAs buffer, GaAs contacts Si-doped to $2 \times 10^{18} \text{ cm}^{-3}$ (1.5 micron bottom contact, 0.5 micron top contact), a superlattice emitter and collector consisting of 50 periods 80 \AA GaAs + 20 \AA $\text{Al}_{0.4}\text{Ga}_{0.6}\text{As}$ Si-doped to $2 \times 10^{18} \text{ cm}^{-3}$ except for 3 undoped periods adjacent to the tunneling barriers, 50 \AA undoped $\text{Al}_{0.4}\text{Ga}_{0.6}\text{As}$ tunnel barriers, and a 150 \AA GaAs quantum well. The center 50 \AA of the quantum well was doped p-type with Be to $1 \times 10^{19} \text{ cm}^{-3}$. The superlattices, AlGaAs barriers, and the quantum well were all grown at 640°C as measured by a short wavelength pyrometer, while the GaAs contacts were grown at 600°C . A cross-section TEM of the structure is shown in Figure 2.

The energy-band profile of the present BiQuaRTT design under a typical bias is shown in Figure 3. The model from which this figure was obtained finds the self-consistent solution of Poisson's equation for the electrostatic potential. The electrons in the contacts are treated in a finite-temperature Thomas-Fermi approximation (i.e. these electrons are assumed to be in local equilibrium with the Fermi levels established by their respective electrodes.) The superlattice layers are represented as homogeneous alloys, the effective composition (of 0.07) determined by solving an envelope wavefunction approximation for the superlattice minibands. The confined

holes in the base are treated quantum-mechanically by solving Schroedinger's equation for the ground state and multiplying the resulting probability density by the Fermi distribution. In the present simulation the base is biased to +1.42 V to pull the quantum well potential down to the vicinity of that of the emitter.

Devices were fabricated using contact lithography, lift-off metallization processes, and implantation. To form a low resistance contact to the quantum well, a triple Be-implant was used consisting of consecutive doses of $1 \times 10^{15} \text{ cm}^{-2}$ at 30, 80, and 160 keV. A rapid thermal anneal at 750 C for 10 s was sufficient to activate the anneal. Ohmic contact to the base was achieved with Ti/Pt/Au, while a Ni/Ge/Au composite formed the collector and emitter contacts. A shallow etch was performed between the emitter and base (implanted contact) to improve isolation between these two contacts. A Si_3N_4 passivation layer was deposited over the entire structure.

Figure 4 shows the common emitter characteristics (current bias) I_C versus V_{CE} of a typical BiQuaRTT structure at room temperature. It should be noted that negative differential resistance should not be observable in this structure if indeed the contact to the quantum well is obtained and the well is not depleted. Typical current gains of 50 are observed, though a singular device exhibited a current gain of 450.

The distinguishing characteristic of this structure is that transport is determined by tunneling through the quantum well states that are biased into resonance by the base potential. Because the quantum well potential is controlled by the base voltage, the familiar signiature of a negative differential resistance for a resonant tunneling diode appears as a negative transconductance in this structure. Figure 5 shows the common emitter characteristics, voltage bias, of the same device shown in Figure 4. The inset to the figure shows the transconductance, which becomes negative at $V_B = 1.1\text{V}$. The negative transconductance values shown here are typical; values as high as -4.0 mS (for similar $5 \mu\text{m}$ square mesas) have been

observed. It should be noted that the maximum current density of $5.6 \times 10^3 \text{ A/cm}^2$ (i.e., before the transconductance becomes negative) is approximately the same as the current density of this resonant tunneling peak observed in a control structure identical except for the p-type quantum well doping.

An important characteristic shown in Figure 5 is that the transconductance asymptotically becomes positive (for $V_B > 1.25\text{V}$). This is due to initiation of resonant tunneling through the next excited state of the quantum well. Parasitic base leakage current (for which Figure 5 has been corrected) of the implanted pn junction prevented observation of further transconductance peaks due to tunneling through higher excited states. Properly designed structures, such as those utilizing InGaAs quantum wells (for larger dynamic range) should allow structures with multiple transconductance peaks.

In summary, a new three-terminal resonant tunneling structure in which current transport is controlled by directly modulating the potential of the quantum well has been demonstrated. Typical current gains of 50 at room temperature and transconductance indicative of resonant tunneling through quantum well states is observed.

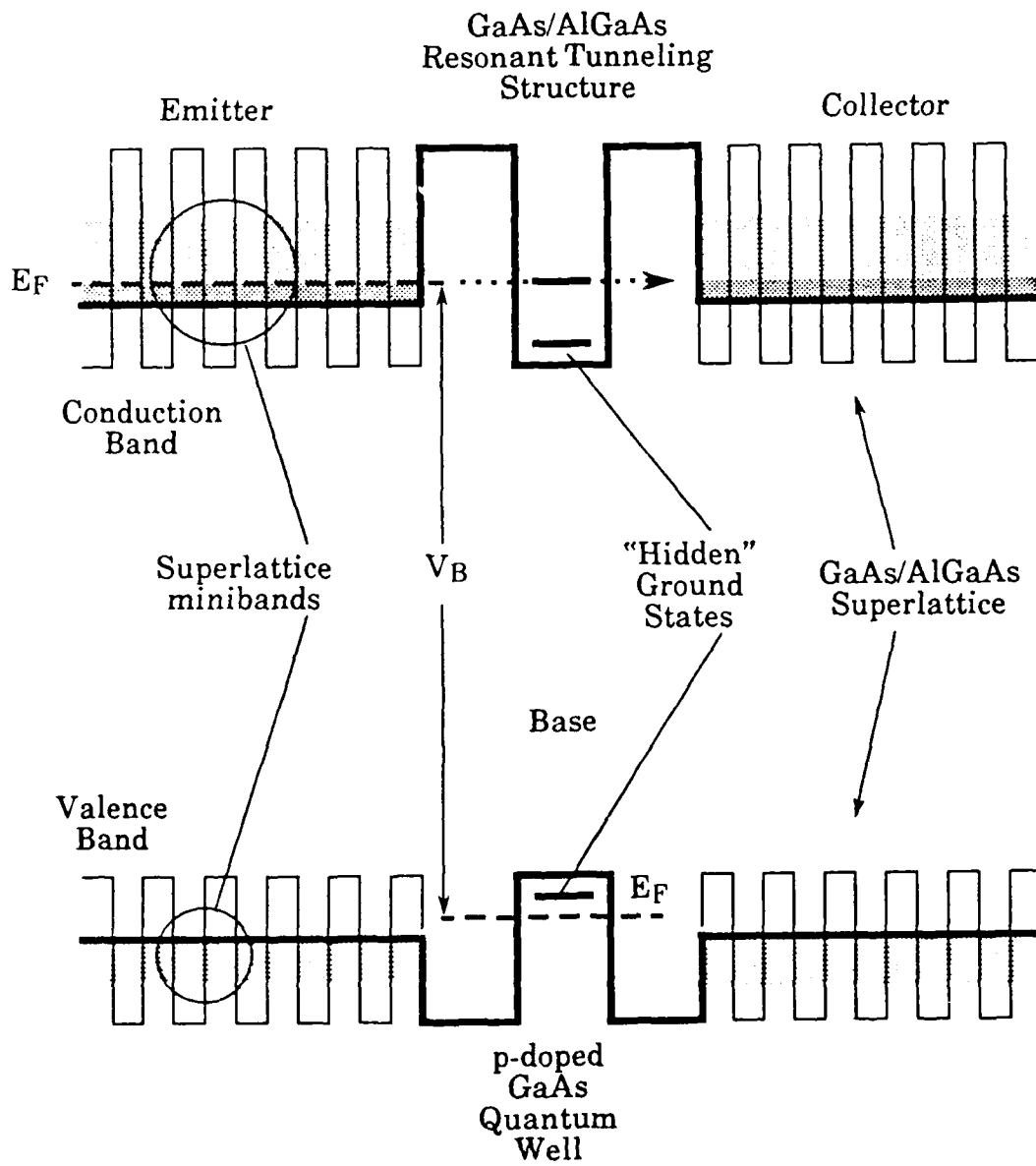
This work was supported by the Air Force Wright Aeronautical Laboratories. We are indebted to R. T. Bate for constant support and encouragement, to B. Bayraktaroglu, B. Kim, F. Morris, D. Plumpton, and C.-H. Yang for discussions, and to Pam Stickney, Frank Stovall, and Randy Thomason for technical assistance.

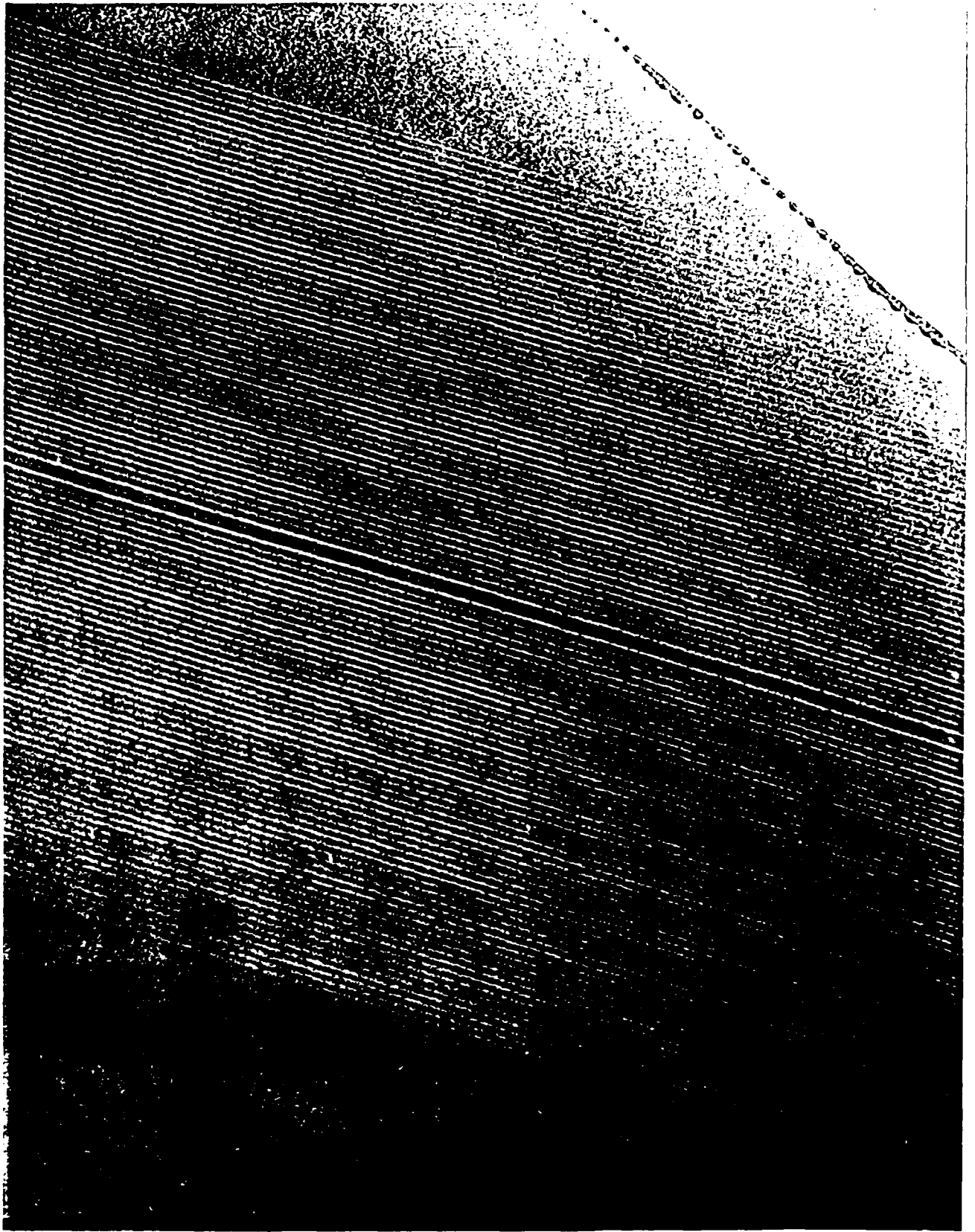
REFERENCES

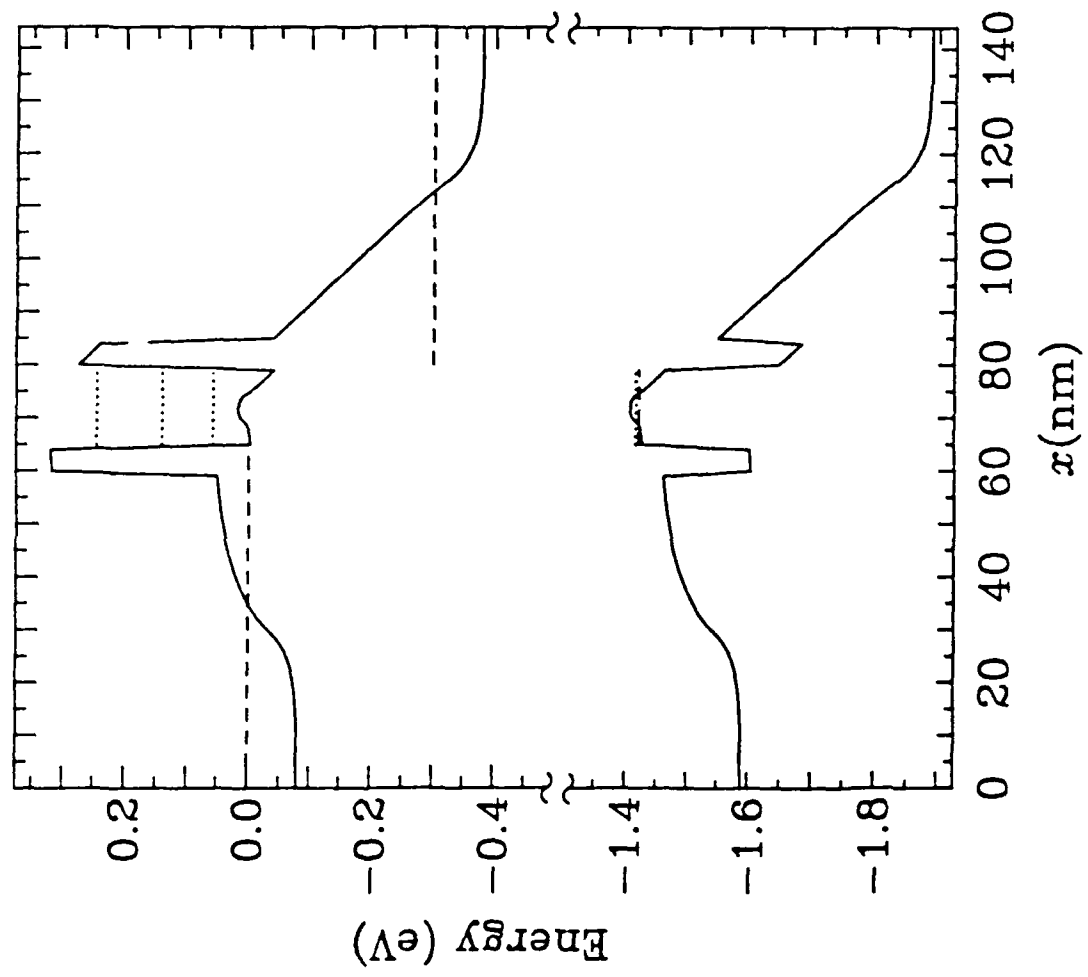
1. L. L. Chang, L. Esaki, and R. Tsu, *Appl. Phys. Lett.* **24**, 593 (1974).
2. T. C. L. G. Sollner, W. D. Goodhue, P. E. Tannenwald, C. D. Parker, and D. D. Peck, *Appl. Phys. Lett.* **43**, 588 (1983).
3. F. Capasso and R. A. Kiehl, *Jour. Appl. Phys.* **58**, 1366 (1986).
4. A. R. Bonnefoi, T.C. McGill, and R.D. Burnham, *EDL-6*, 636 (1985).
5. N. Yokoyama, K. Imamura, S. Muto, S. Hiyamizu, and H. Nishi, *Jap. Jour. Appl. Phys.* **24**, L853 (1985).
6. F. Capasso, S. Sen, A. C. Gossard, A. L. Hutchinson, and J. H. English, *EDL-7*, 573 (1986).
7. T. K. Woodward, T.C. McGill and R.D. Burnham, *Appl. Phys. Lett.* **50**, 451 (1987).
8. W. R. Frensley and M.A. Reed, "Three Terminal Tunneling Device and Method," U.S. patent application filed Jan. 30, 1986.
9. M. A. Reed and J. W. Lee, *Appl. Phys. Lett.* **50**, 845 (1987).

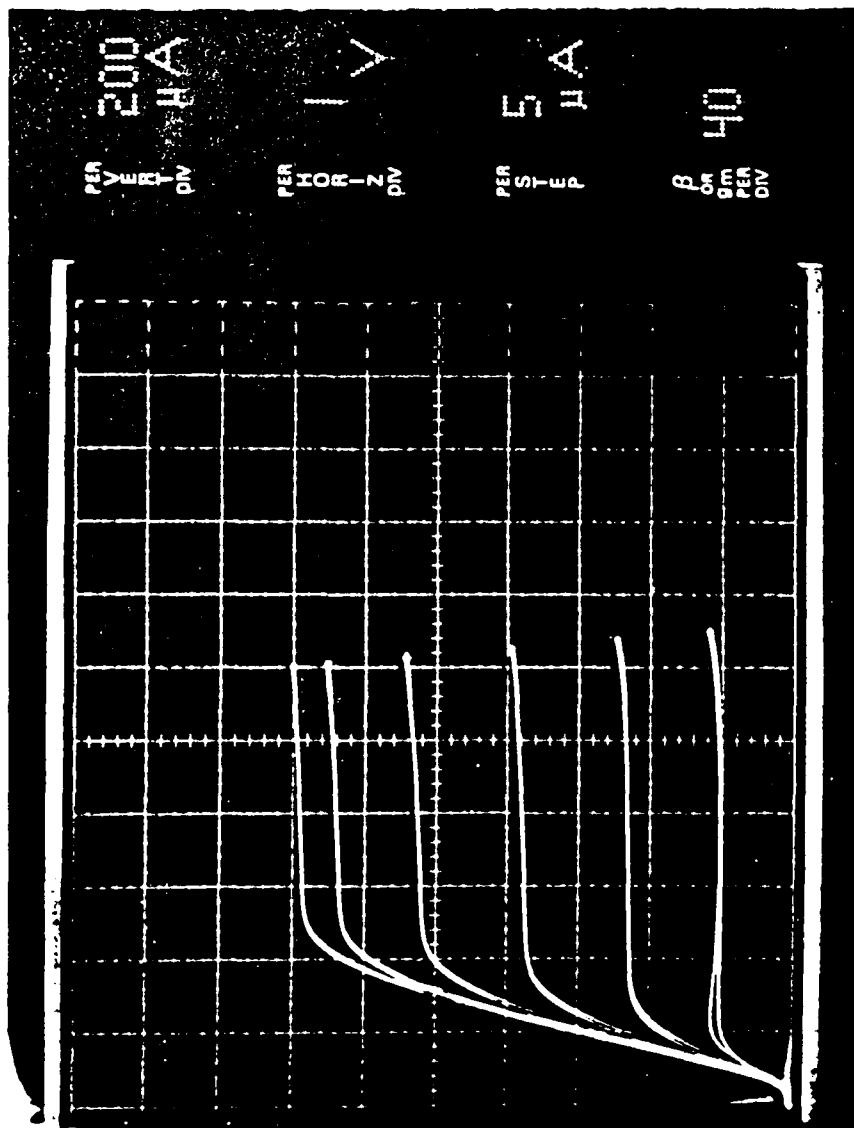
FIGURE CAPTIONS

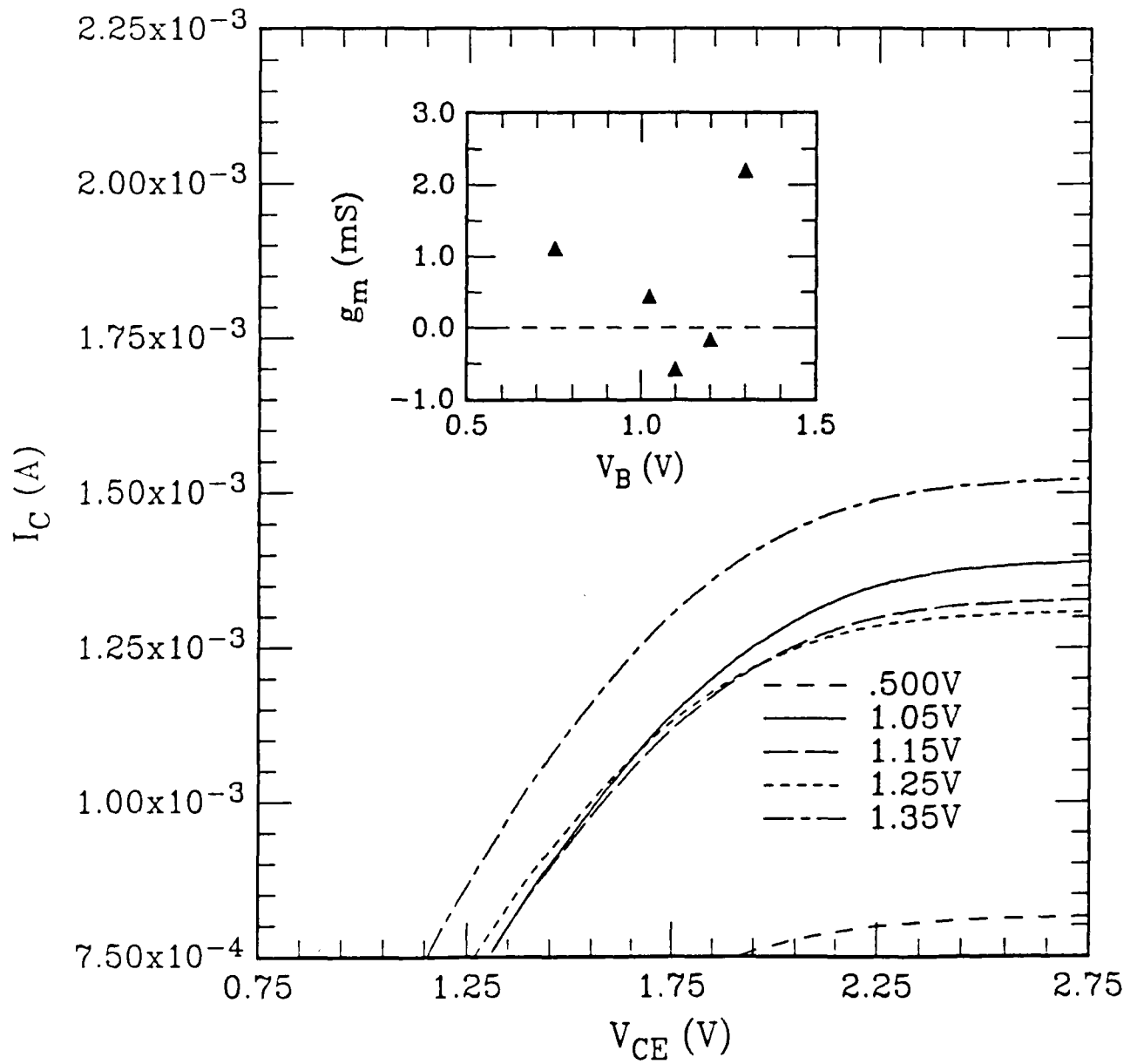
- Figure 1. Schematic bandstructure diagram of the BiQuaRTT. The emitter and collector are superlattices that clad the double barrier resonant tunneling structure, and the base is a p-doped quantum well with a "hidden" ground state.
- Figure 2. Cross section TEM of the superlattice BiQuaRTT structure.
- Figure 3. Energy band profile obtained from a numerical simulation of the present BiQuaRTT structure at 300K with $V_b = 1.42$ V and $V_c = 0.30$ V. The energies of the resonant electron states and the first confined heavy-hole state are shown by dotted lines, and the Fermi levels of the respective electrodes are shown by dashed lines. The presence of a resonant level within a few kT of the emitter Fermi level and the confinement of the hole state are apparent. This simulation neglects current flow, self-consistently solving for the carrier distribution and potential under an assumption of local quasi-equilibrium.
- Figure 4. Common emitter characteristics (current bias) I_C versus V_{CE} of a typical BiQuaRTT structure. Emitter area = $(5 \mu\text{m})^2$, $T = 300\text{K}$.
- Figure 5. Common emitter characteristics (voltage bias) I_C versus V_{CE} of the BiQuaRTT structure shown in Figure 3. Emitter area = $(5 \mu\text{m})^2$, $T = 300\text{K}$. The inset shows the transconductance g_m as a function of base potential V_B . For $1.05\text{V} < V < 1.25\text{V}$, the transconductance is negative.











APPENDIX B

SELECTIVE REACTIVE ION ETCHING OF GaAs ON AlGaAs USING CCl_2F_2 AND HE

Selective reactive ion etching of GaAs on AlGaAs using CCl_2F_2 and He

Alan Seabaugh

Texas Instruments Incorporated, Central Research Laboratories, Dallas, Texas 75265

(Received 2 June 1987; accepted 12 September 1987)

The characteristics of a CCl_2F_2 :He reactive ion etch are reported for use in selectively etching GaAs/AlGaAs heterostructures. The etch is performed at a pressure of 150 mTorr, with rf power of 0.5 W/cm^2 . Both He and CCl_2F_2 flow rates are controlled to 10 sccm, with measured dc self-bias of typically 125 V. The etch rate for GaAs is $1.8 \mu\text{m/min}$, while the AlGaAs etch rate depends on the Al mole fraction x with measured values of 150 \AA/min at $x = 0.28$ and 45 \AA/min at $x = 0.5$. The selectivity is 120 at $x = 0.28$ and 420 at $x = 0.5$. The etch shows an anisotropy between the $\langle 011 \rangle$ and the $\langle 01\bar{1} \rangle$ directions. Measurements of the plasma impedance are reported as a function of pressure, power, and gas flow rate. From these measurements, the dc bias can be computed and is shown to give good agreement with the measured values. The plasma conditions are sensitive to the previous history of the chamber, but by preconditioning the chamber, the etch is readily reproduced.

I. INTRODUCTION

Selective etching techniques simplify the processing of heterostructure devices. In particular, the selective removal of GaAs on AlGaAs has wide application in the fabrication of many exotic and useful device structures. Choosing the etching conditions which lead to the desired etching characteristic, however, is not straightforward, since the etching process depends on many parameters, some of which are not well understood. Here, the properties of the CCl_2F_2 :He etch have been characterized over a region of the plasma parameter space not previously reported. Measurement of the dependence of the dc self-bias on the pressure, power, and flow rates is made to further specify the plasma and to outline the reasons for this choice of plasma conditions.

The characteristics of the CCl_2F_2 (Freon 12) etch on GaAs using a 3-kV dc plasma excitation^{1,2} and using rf excitation,³⁻⁹ have been previously reported. The effects of Ar and O_2 ³ dilution have also been investigated. Similarly, selective etching of GaAs/AlGaAs heterostructures by CCl_2F_2 ⁷⁻⁹ and CCl_2F_2 :He mixtures⁷ with rf excitation has been reported with selectivity as high as 1000 obtained.⁷ Unfortunately, the usually reported conditions for plasma etching, i.e., pressure, gas flow rates (or partial pressure), rf power, and (most of the time) dc self-bias, do not sufficiently describe the etching environment and even these are not always reported. It is shown that a simple method of measuring the plasma impedance^{8,9} can be used to further characterize the plasma conditions. This allows more detailed comparison of plasmas struck in different chamber geometries and may provide insight into how to modify an existing chamber to reproduce a published result.

II. SYSTEM AND PROCEDURE

This work was performed in a planar reactive ion etching (RIE) system utilizing a diffusion pump for evacuating the chamber and a mechanical pump for exhausting the gases. Anodized Al electrodes, 15 cm in diameter, are spaced 3 cm

apart in the chamber. Both top and bottom electrodes are water-cooled with water temperature maintained at 10°C . The 30-cm-diam chamber body is stainless steel with both Pyrex and quartz ports for viewing the plasma. Specimens are loaded by opening an Al lid which makes a Viton O-ring seal with the top of the chamber. A Plasma-Therm 13.56-MHz rf power supply couples through a matching network to the lower electrode. The matching network is positioned against the bottom of the plasma chamber. The gas flow rates are controlled with mass flow meters and the pressure monitored with a capacitance manometer. The helium and Freon 12 are mixed in a stainless-steel manifold before introduction into the chamber. The system base pressure using the cold-trapped mechanical pump is typically $< 10 \text{ mTorr}$, while with the diffusion pump the base pressure is $< 1 \times 10^{-5} \text{ Torr}$. The gas pressure is set manually using a throttle valve between the chamber and the mechanical pump. The chamber is not used solely for CCl_2F_2 -based etches but regularly contains a variety of etching plasmas with no adverse effects.

The GaAs/AlGaAs heterostructures used were grown by molecular-beam epitaxy (MBE); Te-doped and undoped liquid encapsulated Czochralski (LEC) grown GaAs were also etched. All etching was performed on (100) crystal faces. Two Al mole fractions, $x = 0.28$ and 0.5 , were characterized. Patterns were formed in Shipley AZ1350J photoresist for surface profiling with a mechanical stylus. The etch does not visibly attack metallizations (Al, Au) or oxides. Immediately prior to loading, the specimens were soaked in $1\text{HCl}:1\text{H}_2\text{O}$ for 30 s, followed by a 15-s water rinse, and a nitrogen blow dry.

III. PLASMA PARAMETER SELECTION

A selective anisotropic etch with minimal undercut is desirable for our processing applications. The etch needs to leave photoresist intact for subsequent liftoff processing, so a rapid etch rate is desirable to minimize photoresist degradation by the plasma.

To select a fruitful part of the plasma parameter space to focus, the plasma characteristics as a function of pressure, power, and gas flow rates were measured. Because these characteristics can depend on electrode and chamber composition and geometry, published etch results which are reported solely in terms of pressure, power, and flow rates do not completely describe the experimental conditions. As an example, we have tried unsuccessfully to reproduce the etch results of Knoedler and Kuech⁸ (20 mTorr, 0.2 W/cm², CCl₂F₂, 6 sccm). The dc self-bias is a useful figure to use in comparing plasma conditions between systems since it can vary as a function of electrode and chamber material and geometry. In this case, we are able to reproduce the plasma conditions, but the plasma is slightly unstable and the etch rate is an order of magnitude less than their published rate.

We have also tried to reproduce the CCl₂F₂ etching results of Vatus *et al.*⁹ (50 mTorr, 1 W/cm², 2 sccm). Vatus reports a dc self-bias of ~30 V; our system develops a self-bias of 870 V under these conditions. Clearly there are significant differences in our experimental arrangements. We find that insulators placed on the electrodes can significantly decrease the measured self-bias (by charging up, thus suppressing the collection of both ions and electrons and lowering the dc bias). It follows that different electrode materials may also significantly alter the dc bias.

Because several published CCl₂F₂ RIE conditions were not reproduced in our system, we began an investigation of the CCl₂F₂:He plasma first described by Hikosaka *et al.*⁷ The dependence of dc bias on pressure, power, and flow rate for the CCl₂F₂:He plasma is shown in Fig. 1. We chose to examine the CCl₂F₂:He because of the good selectivity shown by Hikosaka *et al.* and our encouraging initial successes with it. The selectivity was shown⁷ to be the highest at low self-bias voltages. From Fig. 1 it can be seen that low dc bias is obtained in our system at higher pressures and lower power. Low flow rates result in decreased GaAs etching⁵ presumably because of the long residence times of the etching gas and its products. The calculated values of dc bias in Fig. 1 were obtained from measurements of the plasma im-

pedance which is discussed next.

van Roosmalen^{10,11} showed that the impedance of the plasma can be calculated from the settings of the matching network between the generator and reactor. Using this method, the measured plasma impedance as a function of pressure, power density, and gas flow rate is shown in Fig. 2. The resistance is represented by the filled circles and refers to the left-hand plot ordinates, the reactance is represented by the open circles and refers to the right-hand plot ordinates; An equivalent circuit picture of the plasma in terms of a series resistance and capacitance can be used to understand the overall plasma characteristics (for more detail see Ref. 11). The central glow of the plasma has a low resistance; electrons and ions are free, with the lighter, more mobile electrons carrying most of the current. In the ion sheaths (dark regions) near the electrodes, a dc potential drop develops to maintain equal ion and electron currents. The dark regions act like a diode, rectifying the rf voltage which appears in large part across it. This picture of the plasma as a series resistance and capacitance has been shown to be a better physical description of the measured plasma impedance than a parallel circuit.¹¹

Referring to Fig. 2, as the pressure increases, the resistance of the plasma increases while the capacitive reactance decreases. From the series equivalent circuit model, as pressure increases, we expect less rf voltage to appear across the dark space capacitance and therefore less dc self bias. This is what is shown in Fig. 1, i.e., that the developed dc bias decreases with increasing pressure. A similar trend is observed in the rf power density dependence. As the rf power density decreases, the resistance of the plasma increases and the capacitive reactance decreases. As before, we expect this to lead to less rf voltage across the dark space capacitance and lower self-bias. In Fig. 1, the dc bias decreases with decreasing rf power density, consistent with the measured impedance and series RC interpretation. Little variation in resistance and reactance is seen as CCl₂F₂ and He flow rates are kept equal and increased. The resistance and capacitive impedance both increase slightly as flow rates increase. Little

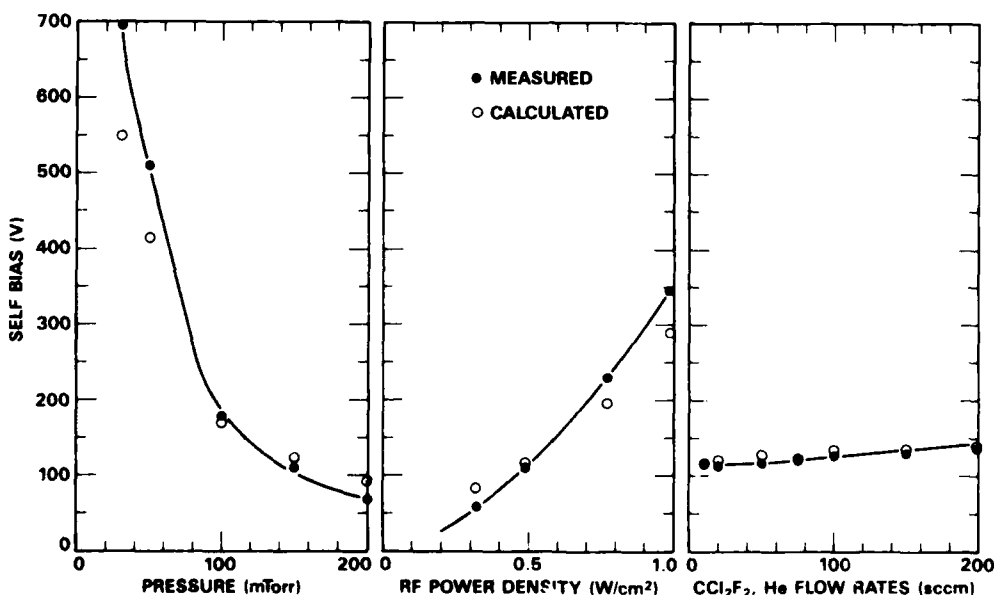


FIG. 1. Dependence of self-bias voltage on (left) pressure with rf power density of 0.5 W/cm² and equal CCl₂F₂ and He flow rates of 10 sccm; (center) rf power density with pressure of 150 mTorr and both CCl₂F₂ and He flow rates of 10 sccm; and (right) equal CCl₂F₂ and He gas flow rates at a pressure of 150 mTorr and a power density of 0.5 W. The filled circles correspond to the measured data while the open circles represent the dc bias calculated from the measured plasma impedance and model of van Roosmalen.

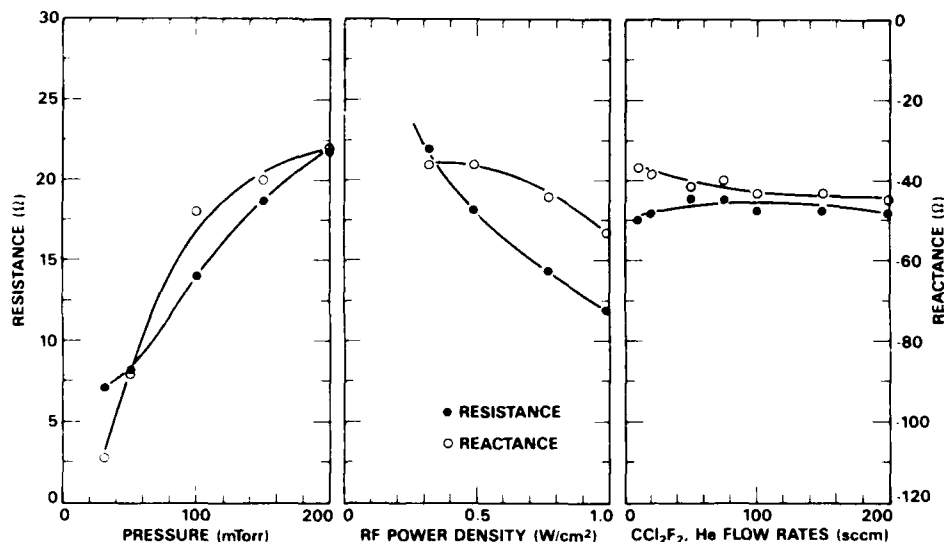


FIG. 2. Dependence of plasma impedance on pressure, rf power density, and gas flow rates as in Fig. 1.

self-bias variation is expected from these impedance measurements or observed in Fig. 1.

It is possible to calculate the dc bias expected from these measurements from the relation¹¹ $V_{dc} = X(2P/R)^{0.5}$, where X is the reactance, R is the resistance, and P is the rms power delivered to the plasma. The results of these calculations appear in Fig. 1 as the open circles. Remarkable agreement is found with deviations apparent at low pressures, Fig. 1 (left), and at high power, Fig. 1 (center).

IV. RESULTS

Shown in Fig. 3 is the dependence of etch depth on time for the GaAs, including both Te- and Cr-doped LEC specimens, and for an MBE-grown 0.8- μm GaAs layer on a thick AlGaAs layer. The etch rate of GaAs is 1.8 $\mu\text{m}/\text{min}$. The GaAs etch rate does not remain linear at long etch times; after 5 min an etch depth of 5.3 μm results corresponding to an average rate of 1.1 $\mu\text{m}/\text{min}$. The etch rate is notably sensi-

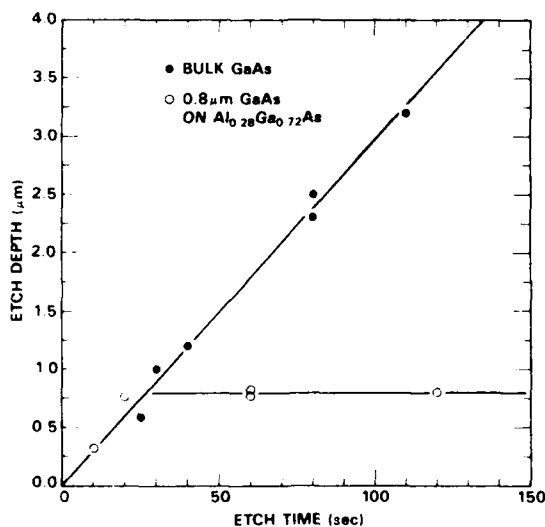


FIG. 3. Dependence of etch depth on etch time for bulk GaAs and an MBE GaAs on AlGaAs heterostructure.

tive to system leaks. The etch rate for this etch was first measured to be 2.8 $\mu\text{m}/\text{min}$, enhanced by a leak from a house nitrogen line into the gas mixing manifold. It is uncertain whether the enhanced etch rate was due to nitrogen or to some other species such as oxygen which has been reported to increase the etch rate of CCl_2F_2 gas.³

To determine the selectivity of the etch, the 0.82- μm GaAs on $\text{Al}_{0.28}\text{Ga}_{0.72}\text{As}$ specimen was etched for 7 min to a depth of 0.92 μm (not shown in Fig. 3). This gives an etch rate of $\text{Al}_{0.28}\text{Ga}_{0.72}\text{As}$ of 150 $\text{\AA}/\text{min}$ and a selectivity of 120. A 100- \AA -GaAs layer on $\text{Al}_{0.5}\text{Ga}_{0.5}\text{As}$ specimen was also etched to determine the etch rate and selectivity. After a 7-min etch of this layer, the etch depth was not greater than 300 \AA . This corresponds to an etch rate of $< 45 \text{\AA}/\text{min}$ and a selectivity of not less than 420. If in fact the etching of AlGaAs slows with time due to the formation of a nonvolatile compound, e.g., AlF_3 , the number obtained for selectivity is somewhat arbitrary and will depend on etch time.

In Fig. 4 a scanning electron microscope (SEM) micrograph of the etched MBE GaAs layer on $\text{Al}_{0.28}\text{Ga}_{0.72}\text{As}$ is shown. The sidewalls are steep and the AlGaAs surface is visibly smooth. The irregular side edge appears to be due to the mask used to pattern this feature, not the etch. When used to etch GaAs, the resulting etch surface is not as

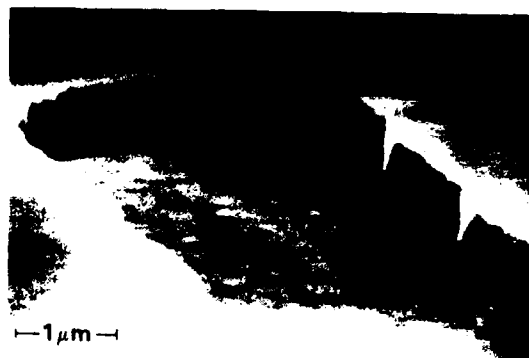


FIG. 4. SEM micrograph of a GaAs layer on an $\text{Al}_{0.28}\text{Ga}_{0.72}\text{As}$ layer

smooth and for an etch of 5 min can have a peak-to-valley roughness of several thousand angstroms.

To determine whether there is a crystallographic anisotropy between the $\langle 011 \rangle$ and $\langle 0\bar{1}\bar{1} \rangle$ directions, a pattern of Al lines was defined on each of two halves of a wafer. On one half of the wafer the lines were oriented parallel to the $\langle 011 \rangle$ direction, while on the other half the lines were oriented parallel to the $\langle 0\bar{1}\bar{1} \rangle$ direction. The specimens were etched 80 s together. An SEM micrograph is shown in Fig. 5. Both sections show an undercut, but the $\langle 0\bar{1}\bar{1} \rangle$ section shows a pronounced lip not observed in the $\langle 011 \rangle$. This is similar to the anisotropy observed in wet acidic hydrogen peroxide etches on GaAs.¹²

One final aspect of this etch needs to be described. We observe that the etch depends on proper conditioning of the system prior to loading specimens. Several other etch gases are used in this same chamber, and this CCl_2F_2 :He etch is sensitive to recent chamber history. Shown in Fig. 6 is the measured dc bias of the plasma as a function of time. Prior to $t = 0$, the system was vented with nitrogen gas to atmospheric pressure, and opened to room air for 1 min. The chamber was then closed and pumped with a mechanical pump to 10 mTorr over 5 min. At this time, defined as $t = 0$, the plasma was struck. From Fig. 6, the plasma takes ~ 1 h to reach a steady state, shown by the circles. If instead of striking the plasma at $t = 0$, the system is pumped by a diffusion pump to 9×10^{-5} Torr in 20 min, and then the plasma is struck, the same curve is followed (see the open circle symbols in Fig. 6). We find that this conditioning or pumping period is necessary in order to achieve reproducible etching. Following this period, the specimens are loaded and the system pumped

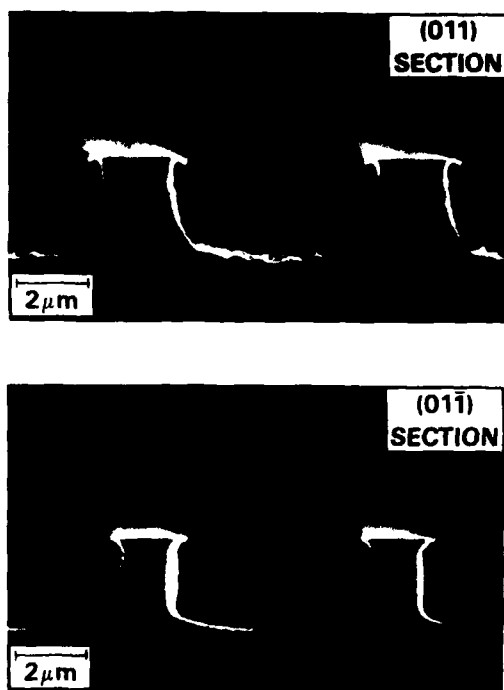


FIG. 5 SEM micrograph of the GaAs etch profile on the $\langle 011 \rangle$ and $\langle 0\bar{1}\bar{1} \rangle$ faces.

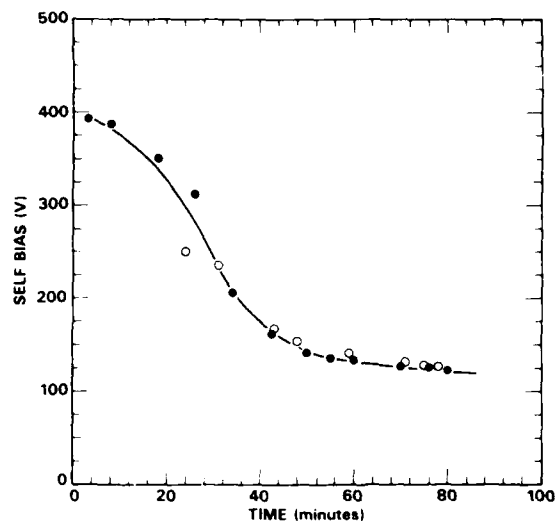


FIG. 6. Self-bias dependence on conditioning time at 150 mTorr, 0.5 W/cm², and equal 10 sccm flow rates for CCl_2F_2 and He: ● no diffusion pumping, ○ diffusion pumped for 20 min prior to striking the plasma.

by a diffusion pump for 20 min. Upon striking the plasma the self-bias is typically 125 V. These results indicate that there is an important chamber conditioning period which must be completed before the plasma reaches a steady rate. We speculate that during this time the electrodes are desorbing products accumulated during previous etches and/or exposure to air. These products alter the collection efficiency of the electrodes for ions and electrons, thus altering the dc bias. The use of a load lock and/or restricting the number of different gases used in the system might eliminate this effect, but as shown here, reproducible etching can be achieved nonetheless.

V. DISCUSSION

Hikosaka *et al.*⁷ note a time delay of nearly 10 s before their CCl_2F_2 :He etch starts. Under the conditions set forth in Fig. 3, however, the etch starts immediately upon striking the plasma. This provides a greater degree of control and obviates the need for striking the plasma at high power densities and subsequently reducing the power to start the etching as Hikosaka *et al.*⁷ suggested. Our etch is performed at a pressure of 150 mTorr while the etch starting delay reported by Hikosaka *et al.* occurred at 37 mTorr. They⁷ suggest that ion sputtering is a necessary mechanism for etch starting, but our findings show that an immediate etch start can also be achieved by increased gas pressure.

To summarize, we have characterized the CCl_2F_2 :He plasma at 150 mTorr, 0.5 W/cm², and equal CCl_2F_2 and He flow rates of 10 sccm. The measured impedance of the plasma can be used to predict the dc self bias with remarkable agreement. We have demonstrated that the etch does show a different anisotropy between the $\langle 011 \rangle$ and $\langle 0\bar{1}\bar{1} \rangle$ directions, but gives a steep wall and planar AlGaAs surface suitable for further device processing. The GaAs etch rate is 1.8 $\mu\text{m}/\text{min}$, yielding short etch times for most device processing steps. Metallizations do not appear to be attacked and

photoresist can still be used for liftoff. The selectivity is a function of the AlGaAs mole fraction, and was found to be 120 for $x = 0.28$ and 450 for $x = 0.5$.

ACKNOWLEDGMENTS

The author would like to thank H.-D. Shih for growing the MBE layers. Helpful discussions with B. Bayraktaroglu, J. N. Randall, D. J. Seymour, and L. C. Witkowski, the technical assistance of G. T. Oliver and J. A. Williams, and editing by J. Fuller are also gratefully acknowledged.

¹R. E. Klinger and J. E. Greene, *Appl. Phys. Lett.* **38**, 620 (1981).

²R. E. Klinger and J. E. Greene, *J. Appl. Phys.* **54**, 1595 (1983).

³E. L. Hu and R. E. Howard, *Appl. Phys. Lett.* **37**, 1022 (1980).

⁴G. Smolinsky, R. P. Chang, and T. M. Mayer, *J. Vac. Sci. Technol.* **18**, 12 (1981).

⁵J. Chaplart, B. Fay, and N. T. Linh, *J. Vac. Sci. Technol.* **B1**, 1050 (1983).

⁶L. G. Hipwood and P. N. Wood, *J. Vac. Sci. Technol.* **B3**, 395 (1985).

⁷K. Hikosaka, T. Mimura, and K. Joshin, *Jpn. J. Appl. Phys.* **20**, L847 (1981).

⁸C. M. Knoedler and T. F. Kuech, *J. Vac. Sci. Technol.* **B4**, 1233 (1986).

⁹J. Vatus, J. Chevrier, P. Delescluse, and J. F. Rochette, *IEEE Trans. Electron Devices* **33**, 934 (1986).

¹⁰A. J. van Roosmalen, *Appl. Phys. Lett.* **42**, 416 (1983).

¹¹A. J. van Roosmalen, W. G. M. van den Hoek, and H. Kalter, *J. Appl. Phys.* **58**, 653 (1985).

¹²D. W. Shaw, *J. Electrochem. Soc.* **128**, 874 (1981).

APPENDIX C

DEFINITIONS/ACRONYMS

Appendix C
DEFINITIONS/ACRONYMS

BIQMODEL	Device modeling program that computes and plots spatially resolved band edges and carrier concentrations in the BiQuaRTT
BiQuaRTT	Bipolar Quantum Resonant Tunneling Transistor
FWHM	Full Width at Half Maximum
MBE	Molecular Beam Epitaxy
Pseudomorphic	Refers to strained layer quantum well structures, i.e., one in which there is a poor match in lattice constant, but the structure is defect-free because the quantum well is so thin
QuESTT	Quantum Excited-State Tunneling Transistor
QUESTTMOD	Device modeling program that computes and plots spatially resolved band edges and carrier concentrations in the QuESTT
RIE	Reactive Ion Etching
RTD	Resonant Tunneling Diode
RTT	Resonant Tunneling Transistor
XPS	X-Ray Photoemission Spectroscopy